







Macrophages and nociceptor neurons form a sentinel unit around fenestrated capillaries to defend the synovium from circulating immune challenge

Received: 4 January 2024

Accepted: 9 October 2024

Published online: 25 November 2024

 Check for updates

Tetsuo Hasegawa ^{1,2} , Colin Y. C. Lee ^{1,3}, Andrew J. Hotchen^{1,4}, Aaron Fleming ¹, Rahul Singh¹, Kunimichi Suzuki⁵, Michisuke Yuzaki ⁵, Masahiko Watanabe⁶, Mark A. Birch⁴, Andrew W. McCaskie⁴, Nikolett Lénárt⁷, Krisztina Tóth⁷, Ádám Dénes⁷, Zhaoyuan Liu⁸, Florent Ginhoux ⁹, Nathan Richoz¹ & Menna R. Clatworthy ^{1,3} 

A wide variety of systemic pathologies, including infectious and autoimmune diseases, are accompanied by joint pain or inflammation, often mediated by circulating immune complexes (ICs). How such stimuli access joints and trigger inflammation is unclear. Whole-mount synovial imaging revealed PVI⁺ fenestrated capillaries at the periphery of the synovium in the lining–sublining interface. Circulating ICs extravasated from these PVI⁺ capillaries, and nociceptor neurons and three distinct macrophage subsets formed a sentinel unit around them. Macrophages showed subset-specific responses to systemic IC challenge; LYVE1⁺CX₃CR1⁺ macrophages orchestrated neutrophil recruitment and activated calcitonin gene-related peptide⁺ (CGRP⁺) nociceptor neurons via interleukin-1 β . In contrast, major histocompatibility complex class II⁺CD11c⁺ (MHCII⁺CD11c⁺) and MHCII⁺CD11c⁻ interstitial macrophages formed tight clusters around PVI⁺ capillaries in response to systemic immune stimuli, a feature enhanced by nociceptor-derived CGRP. Altogether, we identify the anatomical location of synovial PVI⁺ capillaries and subset-specific macrophage–nociceptor cross-talk that forms a blood–joint barrier protecting the synovium from circulating immune challenges.

Synovial joints are the target of antigen-specific autoimmune responses in diseases such as rheumatoid arthritis (RA)¹, but joint pain (arthralgia), or even overt inflammation, is a relatively common manifestation of viral and bacterial infections in distant unrelated organs (for example, bacterial enteritis or streptococcal pharyngitis). This phenomenon is thought, at least in part, to be mediated by circulating microbial antigen–IgG immune complexes (ICs)^{2–4}. Similarly, in systemic lupus erythematosus, an autoimmune disease characterized by IgG IC deposition,

arthritis is a common symptom⁵. Thus, synovial joints act as a ‘barometer’ of systemic inflammation, manifesting as arthralgia or arthritis.

The synovial membrane lines the joint cavity, is the source of synovial fluid and contains several fibroblast and macrophage subsets^{6,7}. It is highly vascular, supplies oxygen and nutrients to adjacent avascular articular cartilage and contains pain fibers^{8–12}. The synovium is also involved in joint pathology, with proliferative pannus arising at the synovia–bone interface, eroding bone in RA^{13–15}.

A full list of affiliations appears at the end of the paper.  e-mail: th647@cam.ac.uk; mrc38@medschl.cam.ac.uk

There is increasing interest in the interplay between neuronal signals and tissue immune cells^{16–18}, but whether or how the triggering of arthralgia-generating pain neurons in response to circulating stimuli is influenced by synovial immune cells or how immune cells in turn might be affected by pain is currently unknown. Here, we established a whole-mount imaging system for the synovium to gain a comprehensive understanding of the spatial organization of the constituent immune, vascular and neuronal components. We investigated the responses of these components to circulating stimuli and addressed the question of why joints are responsive to many systemic pathologies.

Results

PV1⁺ fenestrated capillaries at the periphery of the synovium allow access to circulating stimuli

To interrogate the synovial vasculature via which circulating stimuli gain access to the synovium, we analyzed endothelial cells from single-cell RNA-sequencing (scRNA-seq) data of mouse synovium⁶ (Extended Data Fig. 1a). Genes encoding adhesion molecules, such as *Sele*, *Selp* and *Icam1*, were mainly expressed on *Ackr1*⁺ postcapillary venules, where immune cells extravasate¹⁹ (Extended Data Fig. 1b). Capillary endothelial cells were also evident and, when considered in isolation, comprised two subsets (Fig. 1a). *Plvap* was exclusively expressed in cluster 1 and was among the top ten differentially expressed genes (DEGs) when comparing these two capillary cell clusters (Fig. 1b,c and Extended Data Fig. 1c). PV1 (encoded by *Plvap*) is a molecular component of fenestrated diaphragms, conferring vascular permeability^{20,21}, and its expression is indicative of fenestrated capillaries.

The synovium can be divided into a lining layer containing synovial fibroblasts, with overlying macrophages that interface with the synovial cavity, and a sublining layer with additional macrophage populations^{7,22–24}. Sagittal section imaging showed that PV1⁺ capillaries were specifically located at the interface of the lining and sublining layers, termed hereafter as the lining–sublining (L–SL) interface (Fig. 1d). Although sagittal sections have been used as the gold standard to define the spatial organization of synovial cells, this method provides a limited snapshot of the synovial membrane as a whole, which stretches around the entire joint. Indeed, our knowledge of the global arrangement of synovial cells, particularly in homeostasis, is surprisingly rudimentary. To address these limitations, we developed a protocol to stereotactically dissect the entire synovium of knee joints (Fig. 1e and

Extended Data Fig. 1d,e) and combined whole-mount synovial imaging with an iterative bleaching and staining protocol²⁵ to enable multiparameter imaging. This revealed a dense PV1⁺ vascular network in the sublining layer and confirmed that PV1 was predominantly expressed on capillaries at the L–SL interface (Fig. 1f and Extended Data Fig. 1f). When considering the L–SL interface across the entire area of the synovium, we found that PV1⁺ capillaries were not uniformly distributed but rather were abundant at the periphery of the synovium in proximity to adjacent bones (Fig. 1g).

To test the functional importance of the distribution of PV1 capillaries, we administered 70-kDa and 2,000-kDa dextran intravenously (i.v.) and collected organs 1 h later. Although 70-kDa dextran highly extravasated at the diaphysial side of the growth plate in bone marrow, 2,000-kDa dextran was evident in the synovium (Fig. 1h,i and Extended Data Fig. 1g,h), predominantly in the L–SL interface (Fig. 1j,k). Similarly, i.v. administration of fluorescently labeled microbeads showed that 0.2- μ m microbeads extravasated exclusively from PV1⁺ capillaries in the L–SL interface in the periphery of healthy synovium (Fig. 1l), whereas 2- μ m microbeads were excluded (Extended Data Fig. 1i). Finally, we used a clinically relevant challenge; i.v. ICs (ovalbumin (OVA) opsonized with a polyclonal anti-OVA IgG²⁶) also extravasated into the local synovial tissue from PV1⁺ capillaries (Fig. 1m,n). Together, these data indicate that circulating stimuli readily gain access to the healthy synovium via highly permeable PV1⁺ capillaries located at the L–SL interface in the periphery of the synovium.

Three subsets of macrophages with distinct distribution patterns line synovial PV1⁺ capillaries

We next sought to interrogate which immune cells localized to these sites of potential vulnerability around PV1⁺ capillaries. ERTR7⁺ lining fibroblasts evident in sagittal sections (Fig. 2a) formed a uniform, tightly knit lining layer in the synovial whole-mount images (Fig. 2b), but CD68⁺ macrophages showed increased density in the periphery of the synovium (Fig. 2b and Extended Data Fig. 3a). No extravascular synovial T or B cells were detectable (Fig. 2c). We therefore focused on further characterizing the synovial macrophage populations.

scRNA-seq data showed that synovial macrophages (*Cd68*⁺*Adgre1*⁺) can be divided into a *Cx3cr1*⁺ population (previously described as lining macrophages⁷), which also express *Lyve1*, *Timd4* and *Folr2*, an *H2-Ab1*⁺ population (previously described as interstitial macrophages⁷)

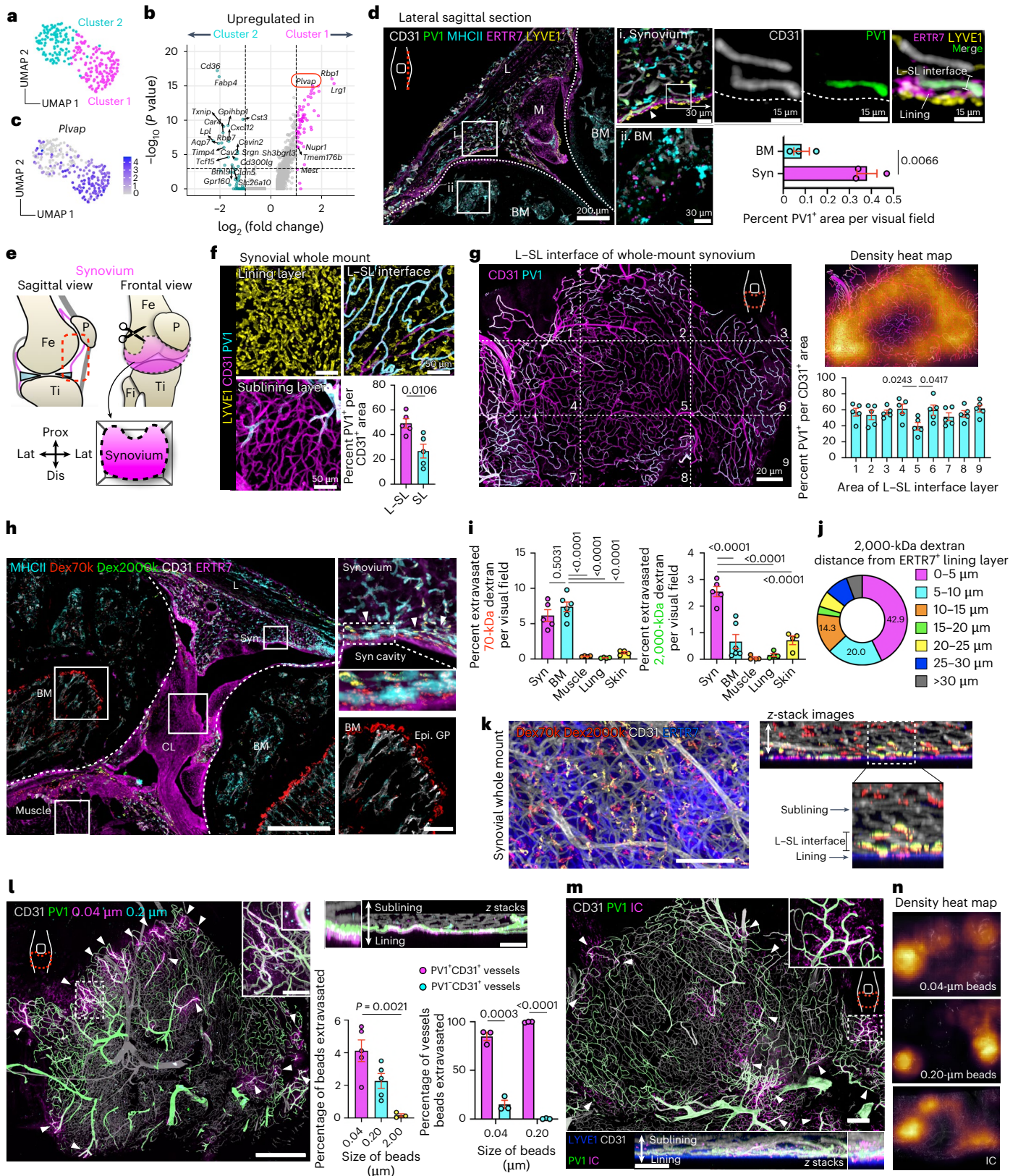
Fig. 1 | PV1⁺ fenestrated capillaries in the L–SL interface at the peripheral area of the synovium allow circulating stimuli to access the synovium.

a, Uniform manifold approximation and projection (UMAP) visualization of synovial capillary endothelial cells extracted from CD31⁺ endothelial cells (Extended Data Fig. 1a,b). scRNA-seq data are from GSE145286. **b**, Volcano plots showing DEGs between two clusters of synovial capillary endothelial cells. **c**, UMAP visualization of synovial capillary endothelial cells expressing *Plvap*. Color bar shows the expression level. **d**, Representative confocal images of sections of knee joints; BM, bone marrow; M, meniscus; L, patella ligament; Syn, synovium; $n = 3$ mice for each group. **e**, Schematic diagram showing the protocol to dissect whole synovium from knee joints. The red dashed outline indicates the area of synovium dissected. Fe, femur; Ti, tibia; P, patella; Fi, fibula; Prox, proximal; Lat, lateral; Dis, distal. **f**, Three-dimensional reconstruction of representative confocal images of the indicated layer of whole-mount synovium. Quantification of the PV1⁺ area among CD31⁺ area at the indicated layers is shown on the bottom right; $n = 5$ mice for each group. **g**, Three-dimensional reconstruction of representative confocal images and density map of the L–SL interface of whole-mount synovium. Quantification of the PV1⁺ area among CD31⁺ area at the indicated compartments is shown on the bottom right; $n = 5$ mice. **h**, Representative confocal images of sections of knee joints from WT mice injected i.v. with 70- and 2,000-kDa dextran (300 μ g of 70-kDa dextran (Dex70k) and 150 μ g of 2,000-kDa dextran (Dex2000k)) 1 h before analysis. Arrowheads indicate the area where 70- and 2,000-kDa dextran merged; CL, cruciate ligament; Epi. GP, epiphyseal growth plate; scale bars, 500 and 100 μ m (inset). **i**, Quantification of the extravasated area in each tissue; $n = 4$ to 6 mice

for each group. **j**, Pie graph showing the percentage of distance between 2,000-kDa dextran and the ERTR7⁺ lining layer of the synovium in the section images; $n = 4$ mice. **k**, Three-dimensional reconstruction of representative confocal images of whole-mount synovium from WT mice injected i.v. with 70- and 2,000-kDa dextran 1 h before analysis; scale bar, 100 μ m. **l**, Three-dimensional reconstruction of representative confocal images of whole-mount synovium from WT mice injected i.v. with fluorescently labeled microbeads of different sizes (25 μ l of each FluoSphere carboxylate-modified microsphere dissolved in PBS) 1 h before analysis. Arrowheads indicate the sites where microbeads extravasated; scale bars, 500 and 50 μ m (inset). Quantification of the area and capillary microbeads extravasated is shown on the bottom right; $n = 3$ to 5 mice for each group. **m**, Three-dimensional reconstruction of representative confocal images of whole-mount synovium from WT mice injected i.v. with OVA–AF647; rabbit polyclonal anti-OVA (RaOVA) ICs (40 μ g of OVA–AF647 + 150 μ g of RaOVA) 2 h before analysis. Arrowheads indicate sites where ICs extravasated; scale bars, 200 and 100 μ m (z-stack images). **n**, Density map of a three-dimensional reconstruction of representative confocal images of whole-mount synovium from WT mice injected i.v. with microbeads or ICs. Data in **d**, **f** and **l** (right) were analyzed by two-tailed *t*-test. The center compartment was used as a control group in one-way analysis of variance (ANOVA) with a Dunnett's test for **g**. Data in **i** and **l** (left) were analyzed by one-way ANOVA with Tukey's post hoc test, and data in **b** were analyzed by two-tailed Wilcoxon rank-sum test. Data in **d**, **f**, **g**, **i** and **l** are shown as mean \pm s.e.m. Images in **k**, **m** and **n** are representative of at least three independent experiments with similar results.

and a subpopulation within the *H2-Ab1*⁺ population expressing *Itgax* (encoding CD11c; Extended Data Fig. 2a–c). Unsupervised assessment of myeloid surface markers using flow cytometry also showed that myeloid cells in the healthy synovium can be divided into major histocompatibility complex class II⁺CD11c⁻ (MHCII⁺CD11c⁻), MHCII⁺CD11c⁺ and MHCII⁻LYVE1⁺ clusters, which also express CX₃CR1

(Extended Data Fig. 2d,e). These data informed the gating strategy subsequently used in our study characterizing three subsets of synovial macrophages, CD11c⁺IAIE(MHCII)⁺, CD11c⁻MHCII⁺ and MHCII⁻LY6C⁻LYVE1⁺CX₃CR1⁺ cells, which were phenotypically and morphologically distinct (Fig. 2d). MHCII⁻LYVE1⁺ macrophages expressed CX₃CR1 and TIM4, whereas CD206 and CD64 were expressed in all three populations.



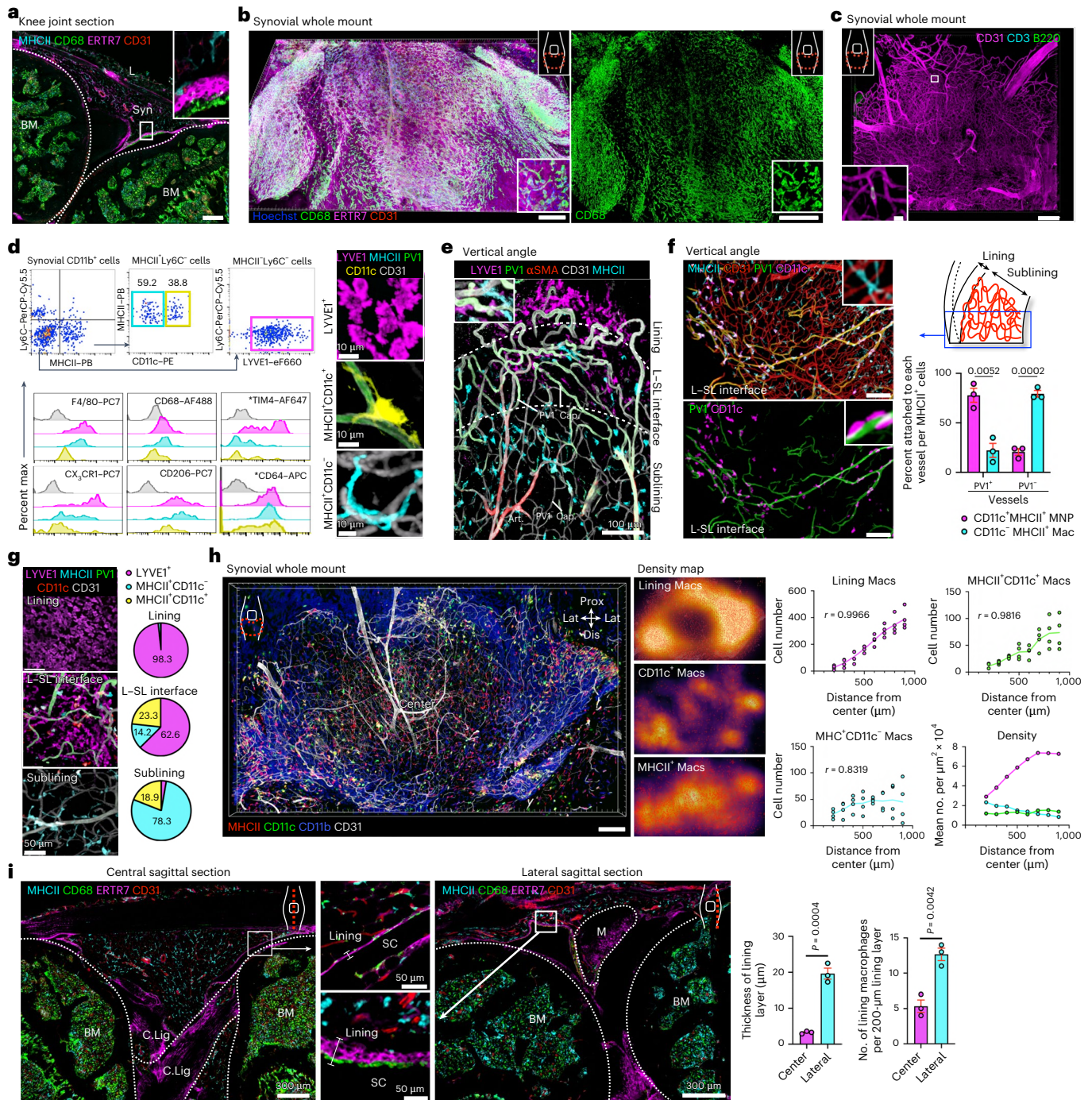


Fig. 2 | Three subsets of macrophages with distinct distribution patterns line synovial PVI⁺ capillaries. **a**, Representative confocal images of sections of healthy knee joints; BM, bone marrow; Syn, synovium; L, patella ligament; scale bar, 200 μ m. **b**, Three-dimensional reconstruction of representative confocal images of whole-mount synovium; scale bars, 200 (left) and 300 μ m (right). **c**, Three-dimensional reconstruction of representative confocal images of whole-mount synovium; scale bars, 200 and 10 μ m. **d**, Gating strategy and flow cytometric analysis of three subsets of synovial macrophages with indicated cell surface markers. Shaded regions indicate staining with isotype controls. Data are representative of at least two independent experiments with similar results. The asterisks (*) indicate that fluorophores for LYVE1 were changed to apply the indicated antibodies. Representative confocal images of each subset of macrophages are shown on the right. **e**, Three-dimensional reconstruction of representative confocal images of whole-mount synovium from a vertical angle. The two dashed lines are (1) the border of lining layer and L-SL interface, and (2) L-SL interface and sublining layer. Cap., capillary; Art., arteriole.

f, Three-dimensional reconstruction of representative confocal images of whole-mount synovium from a vertical angle; scale bars, 100 μ m. Quantification of the percentage of CD11c⁺MHCII⁺ and CD11c⁺MHCII⁻ macrophages (Mac) attached to PVI⁺CD31⁺ or PVI⁻CD31⁺ vessels; $n = 3$ mice for each group. Data represent mean \pm s.e.m. **g**, Three-dimensional reconstruction of representative confocal images at the indicated layers of whole-mount synovium. The pie graphs show the percentages of the three types of macrophages in the indicated layers of the synovium; $n = 3$ mice. **h**, Three-dimensional reconstruction of representative confocal images of whole-mount synovium (left) and density maps of three subsets of macrophages (middle); scale bar, 200 μ m. The numbers and densities of each macrophage type in the indicated compartment of the synovium are shown on the right; $n = 4$ mice for each group. **i**, Representative confocal images of sections of healthy knee joints; M, meniscus; C.Lig, crescent ligament; SC, synovial cavity; $n = 3$ mice for each group. Data represent mean \pm s.e.m. Data in **f** and **i** were analyzed by two-tailed *t*-test. Images in **a–e** are representative of at least two independent experiments with similar results.

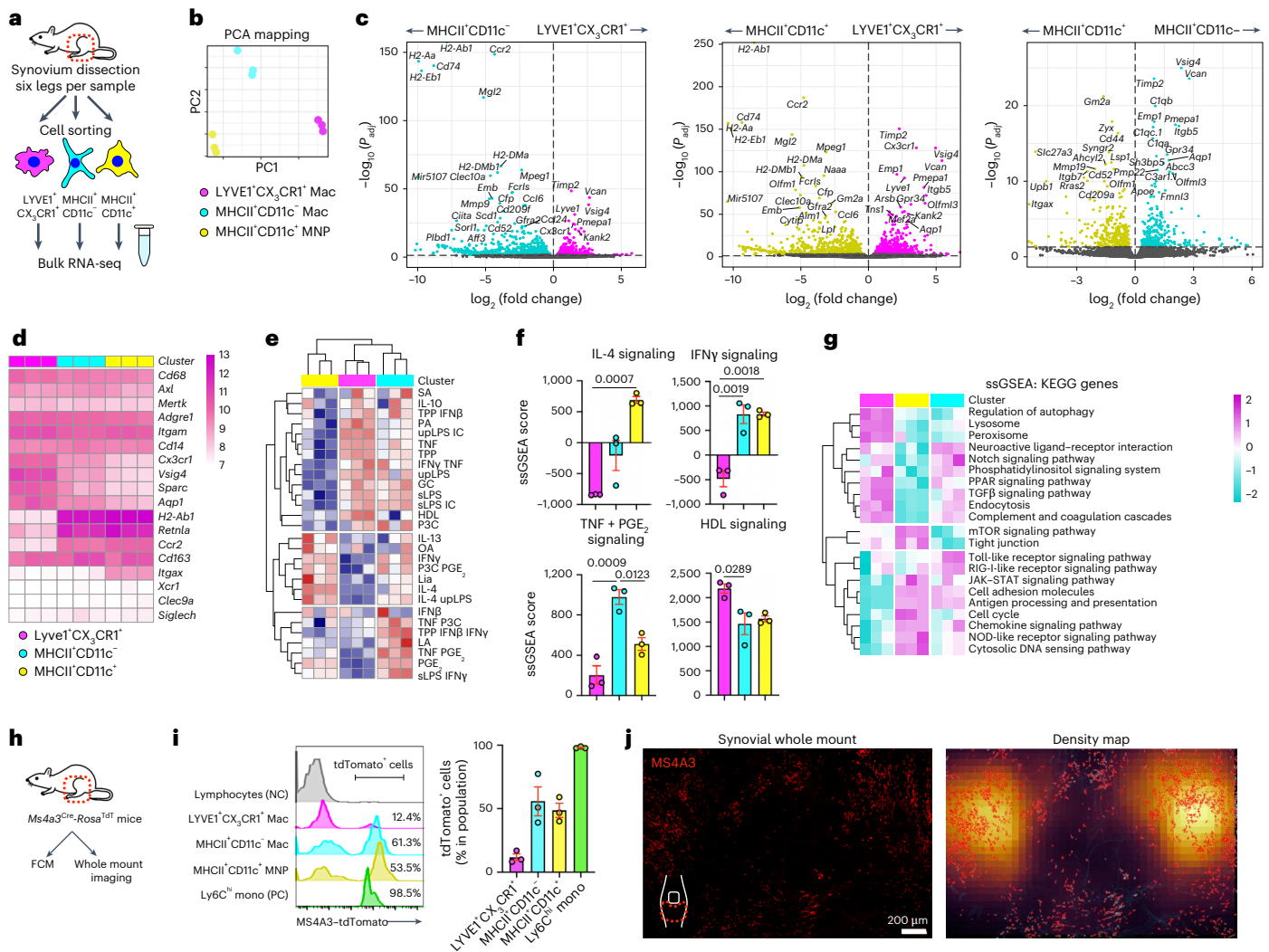


Fig. 3 | Three subsets of synovial macrophages show distinct transcriptomes and ontogenies. **a**, Illustration of the experimental protocol. **b**, Principal component analysis (PCA) of three subsets of synovial macrophages by RNA-seq; $n = 3$ mice for each plot and $n = 9$ mice for each population. **c**, Volcano plots showing DEGs between LYVE1⁺CX₃CR1⁺, MHCII⁺CD11c⁻ and MHCII⁺CD11c⁺ macrophages from WT mice; P_{adj} , adjusted P value. **d**, Heat map of the expression of canonical macrophage genes (normalized values) and dendritic cell markers in LYVE1⁺CX₃CR1⁺, MHCII⁺CD11c⁻ and MHCII⁺CD11c⁺ macrophages from bulk RNA-seq analysis. **e**, Heat map of single-sample gene set enrichment analysis (ssGSEA) of three synovial macrophage subsets by RNA-seq. The signature genes from a previously published dataset (Xue et al.²⁷) describing the transcriptional programs activated with 28 different stimuli were used; TPP, TNF+PGE₂+P3C; IFN, interferon; PA, palmitic acid; LPS, lipopolysaccharide; TNF, tumor necrosis factor; GC, glucocorticoid; HDL, high-density lipoprotein; P3C,

Pam3CysSerLys4; OA, oleic acid; Lia, linoleic acid; LA, lauric acid; sLPS, standard lipopolysaccharide; upLPS, ultrapure lipopolysaccharide. **f**, Quantification of ssGSEA scores for signaling pathways of the indicated stimuli for each subset; $n = 3$ mice for each plot and $n = 9$ mice for each population. Data represent mean \pm s.e.m. **g**, Heat map of ssGSEAs of three synovial macrophage subsets with KEGG enrichment analysis (scaled normalized values). **h**, Illustration of the experimental protocol; FCM, flow cytometry. **i**, Flow cytometric analysis of MS4A3-tdTomato positivity of the indicated macrophage subsets from 10-week-old mice; $n = 3$ mice for each group. Data represent mean \pm s.e.m.; NC, negative control; mono, monocytes; PC, positive control. **j**, Three-dimensional reconstruction of representative confocal images of whole-mount synovium and density map of MS4A3-tdTomato. Images are representative of three animals with similar results. Data in **f** were analyzed by one-way ANOVA with Tukey's post hoc test, and data in **c** were analyzed by Wald test.

To investigate the spatial distribution of macrophages relative to PVI⁺ capillaries, we performed whole-mount synovial imaging vertically at the edge of whole-mounted synovium. This showed that α -smooth muscle actin⁺ (α SMA⁺) arterioles give rise to PVI⁺ capillaries at the L-SL interface, which were surrounded by LYVE1⁺ macrophages (Fig. 2e). CD11c⁻MHCII⁺ macrophages lined both PVI⁻ and PVI⁺ vasculature, whereas CD11c⁺MHCII⁺ mononuclear phagocytes (MNP) specifically localized to PVI⁺ vessels (Fig. 2f). Therefore, all three macrophage subsets were found in proximity to PVI⁺ capillaries in the L-SL interface (Fig. 2g). When considering the synovium as a whole, lining macrophages varied in their distribution density, with far fewer cells in the central region (Fig. 2h). In the sublining layer, CD11c⁻MHCII⁺ MNPs

predominantly localized in the periphery, whereas CD11c⁻MHCII⁺ macrophages were uniformly distributed throughout the synovium (Fig. 2h). Sagittal sections confirmed that the density of lining macrophages and the thickness of the lining layer were significantly greater at the peripheral area near the meniscus between the femur and tibia than at the central area (Fig. 2i).

Bulk RNA-seq of the sorted macrophage subsets showed that they were transcriptionally distinct, with LYVE1⁺CX₃CR1⁺ macrophages expressing markers of lining macrophages (*Cx3cr1*, *Vsig4* and *Sparc*) and CD11c⁺MHCII⁺ and CD11c⁻MHCII⁺ macrophages demonstrating transcriptional similarity to interstitial macrophages (*H2-Ab1* and *Retnla*; Fig. 3a-d). Compared to reference transcriptional

signatures obtained from macrophages activated with different stimuli²⁷. CD11c⁺MHCII⁺ MNP were enriched for gene sets associated with M2 stimuli (interleukin-4 (IL-4) and IL-13), whereas LYVE1⁺CX₃CR1⁺ macrophages were enriched for tumor necrosis factor (TNF) and high-density lipoprotein stimulation signatures (Fig. 3e,f). Pathway analysis showed that LYVE1⁺CX₃CR1⁺ macrophages expressed genes related to endocytosis and the lysosome, whereas the MHCII⁺ subsets were enriched for gene sets related to cell adhesion and antigen processing and presentation (Fig. 3g).

We next investigated the kinetics of synovial macrophage replenishment by circulating monocytes using *Ms4a3*^{Cre}-*Rosa*^{TdTomato} mice. *Ms4a3* is specifically expressed by granulocyte–monocyte progenitors, and this model efficiently fate maps monocytes and granulocytes but not lymphocytes or tissue dendritic cells²⁸. In accordance with published reports showing that MHCII⁺ macrophages are replaced faster than MHCII⁺ macrophages in other organs²⁸, in the synovium, almost half of MHCII⁺ macrophages were tdTomato⁺, whereas most of LYVE1⁺CX₃CR1⁺ macrophages were tdTomato⁻ (Fig. 3h,i). An equivalent proportion of MHCII⁺CD11c⁺ MNPs were tdTomato⁺ compared to MHCII⁺CD11c⁻ macrophages, indicating that MHCII⁺CD11c⁺ MNPs have an ontogenic profile similar to macrophages rather than dendritic cells. Whole-mount synovial imaging of *Ms4a3*^{Cre}-*Rosa*^{TdTomato} mice showed that tdTomato⁺ cells were predominantly distributed at the periphery of the synovium (Fig. 2j and Extended Data Fig. 3b).

Synovial macrophages sample circulating ICs and present antigens

Given their proximity to PVI⁺ capillaries, we next investigated the capacity of synovial macrophages to take up circulating ICs in vivo. Two hours following i.v. administration, ICs extravasated from PVI⁺ capillaries at the L–SL interface (Fig. 4a,b), and uptake was evident mainly in LYVE1⁺CX₃CR1⁺ macrophages, consistent with a previous report²⁴. CD11c⁺MHCII⁺ and CD11c⁻MHCII⁺ macrophages were also capable of internalizing ICs, with a greater IC uptake than OVA alone (Fig. 4c,d and Extended Data Fig. 3c). Notably, CD11c⁻MHCII⁺ MNPs were also able to internalize and present circulating peptide (Ea; Fig. 4e–g), consistent with their enrichment for antigen processing and presentation gene sets (Fig. 3g).

Because Fcγ receptors (FcγRs) bind to the Fc portion of IgG to mediate the cellular effector responses to ICs, we analyzed their expression in synovial macrophages. Of note, the relative expression of activating receptors (FcγRIII/FcγRIV) and the inhibitory receptor (FcγRIIb) determines the activation threshold of a cell when encountering IgG ICs, termed the A:I ratio (Extended Data Fig. 3d)²⁹. Flow cytometric

analysis showed that LYVE1⁺CX₃CR1⁺ macrophages expressed higher levels of FcγRIIb and FcγRIII than the other two subsets, but FcγRIV expression was absent in synovial macrophages (Fig. 4h). Whole-mount synovium imaging showed FcγRII/FcγRIII expression mostly at the L–SL interface on LYVE1⁺ macrophages (Fig. 4i and Extended Data Fig. 3e,f). Circulating ICs led to downregulation of FcγRIII expression in all three subsets, whereas the expression of the inhibitory receptor (FcγRIIb) was maintained (Fig. 4j), thereby increasing the activation threshold and preventing excessive (and potentially damaging) responses to circulating ICs.

To determine if this microarchitectural arrangement was present in human synovium, we optimized a whole-mount imaging system for human knee joint synovium using clearing-enhanced 3D (Ce3D), a tissue clearing solution (Extended Data Fig. 3g)³⁰. Beneath the CD55⁺ lining layer fibroblasts⁶ (Fig. 4k and Extended Data Fig. 3h), an abundant PVI⁺ capillary network was present (Fig. 4l) and was tightly covered with LYVE1⁺ and HLA-DR⁺ macrophages and some LYVE1⁺ macrophages expressing CD32B (FCGR2B), whereas fat pad capillaries were scantily lined with perivascular macrophages (Fig. 4m,n), analogous to our observations in mouse synovium.

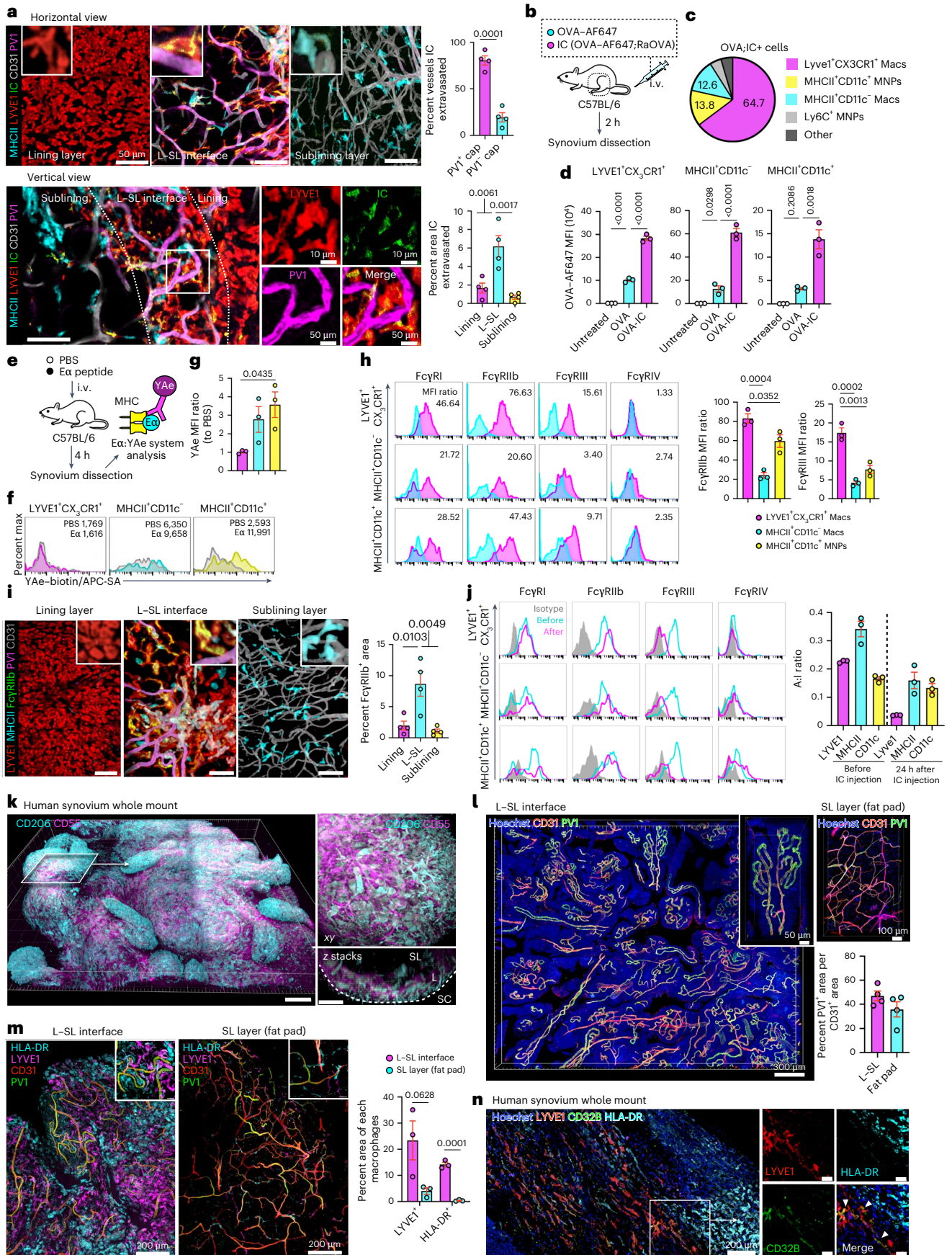
Systemic IC challenge induced distinct responses in synovial macrophage subsets

To further interrogate synovial macrophage responses to ICs, we performed bulk RNA-seq on sorted subsets following i.v. IC challenge in vivo in wild-type (WT) and FCGR2B-deficient (*Fcgr2b*^{-/-}) mice (Fig. 5a). IC challenge was associated with increased *Fcgr2b* expression in LYVE1⁺CX₃CR1⁺ macrophages in WT mice, consistent with a negative feedback loop (Fig. 5b). Less than 3% of DEGs were shared among the three macrophage subsets in both WT and FCGR2B-deficient mice, indicating subset-specific responses to circulating IC challenge (Fig. 5c). CD11c⁺MHCII⁺ and CD11c⁻MHCII⁺ macrophages shared more DEGs, including *Fcgr1*, *Mmp19*, *Irf7* and *Cxcl13*, than LYVE1⁺CX₃CR1⁺ macrophages (Fig. 5c and Extended Data Fig. 4a). Pathway enrichment analysis using upregulated genes showed that LYVE1⁺CX₃CR1⁺ macrophages were enriched with gene sets related to neutrophil migration, whereas CD11c⁺MHCII⁺ macrophages were enriched with gene sets related to cell adhesion and migration after IC stimulation (Fig. 5d).

FcγRIIb deficiency was associated with a greater increase in the number of DEGs in LYVE1⁺CX₃CR1⁺ macrophages than in WT cells (Fig. 5e and Extended Data Fig. 4b), consistent with the high FcγRIIb expression detectable in this population. Because leukocyte activation- and neutrophil migration-associated genes were enriched in LYVE1⁺CX₃CR1⁺ cells after i.v. IC challenge (Extended Data Fig. 4c), we further probed

Fig. 4 | Synovial macrophages sample circulating ICs, and MHCII⁺ macrophages present antigens. **a**, Three-dimensional reconstruction of representative confocal images of the indicated layers and vertical views of whole-mount synovium from WT mice injected i.v. with OVA–AF647;RaOVA (40 μg of OVA–AF647 + 150 μg of RaOVA) 2 h before analysis. Quantification of the percentage of OVA-IC⁺ area within PVI⁺ and PVI⁻CD31⁺ area and the percentage of OVA-IC⁺ area in the lining layer, L–SL interface and sublining layer is shown on the right; *n* = 4 mice for each group. **b**, Schematic diagram showing the protocol. **c**, Pie graph showing the mean percentage of OVA-IC⁺ macrophage subsets among all OVA-IC⁺ cells; *n* = 3 mice. **d**, Scatter plots of mean fluorescence intensity (MFI) of OVA–AF647 and OVA–AF647;RaOVA; *n* = 3 mice for each group. **e**, Schematic diagram showing the protocol of antigen presentation in vivo using the Ea:Yae system. **f,g**, Flow cytometric analysis (**f**) and quantification (**g**) of Yae MFI of the indicated macrophage subsets from mice injected i.v. with Ea divided by that observed in macrophages from mice injected with PBS. Shaded regions indicate mice injected with PBS control; *n* = 3 mice for each group. **h**, Flow cytometric analysis of different types of synovial macrophages with indicated FcγRs. Cyan regions indicate staining with isotype controls. Scatter plots show the MFI ratio of each FcγR and isotype controls on each subset; *n* = 3 mice for each group. **i**, Three-dimensional reconstruction of representative confocal images of the indicated layers of whole-mount synovium; scale bars, 50 μm.

Quantification of the percentage of FcγRIIb⁺ area in the indicated layers is shown on the right; *n* = 4 mice for each group. **j**, Flow cytometric analysis of different types of synovial macrophages with the indicated FcγRs before and 24 h after IC injection. Gray regions indicate staining with isotype controls. The FcγR A:I ratios were calculated according to MFI ratios of activating (FcγRIII and FcγRIV) and inhibitory FcγRIIb before and 24 h after IC injection on each subset; *n* = 3 mice for each group. **k**, Three-dimensional reconstruction of representative confocal images of whole-mount human synovium; scale bars, 100 (left) and 30 μm (right); L, lining layer; SL, sublining layer; SC, synovial cavity. **l**, Three-dimensional reconstruction of representative confocal images of whole-mount human synovium. Quantification of PVI⁺ area among CD31⁺ area in each layer; *n* = 3 individuals for each group. **m**, Three-dimensional reconstruction of representative confocal images of whole-mount human synovium. Quantification of LYVE1⁺ and HLA-DR⁺ area in the visual field is shown on the right; *n* = 3 individuals for each group. **n**, Three-dimensional reconstruction of representative confocal images of whole-mount human synovium; scale bars (right), 100 μm. Images are representative of at least two independent experiments with similar results. The arrowheads indicate the merged area for LYVE1 and CD32B. Data in **a** and **m** were analyzed by two-tailed *t*-test, and data in **d** and **g–i** were analyzed by one-way ANOVA with Tukey's post hoc test. Data in **a**, **d**, **g–j**, **l** and **m** are shown as mean ± s.e.m.



the expression of chemokines. We found a greater IC-induced upregulation of the neutrophil-recruiting chemokine *Cxcl1* in LYVE1⁺CX₃CR1⁺ and CD11c⁺MHCII⁺ macrophages in *Fcgr2b*^{-/-} mice than in WT mice (Fig. 5f,g and Extended Data Fig. 4d), supporting the conclusion that FcγRIIb is important for limiting neutrophil entry after IC challenge. We confirmed a significant increase in CXCL1 and CXCL2 protein expression and infiltrating neutrophils within the synovium of *Fcgr2b*^{-/-} mice following i.v. IC challenge (Fig. 5h–j).

Interestingly, given the enrichment of cell adhesion and migration gene sets in activated CD11c⁺MHCII⁺ macrophages, we occasionally noted clusters of MHCII⁺ macrophages tightly entwined around PVI⁺ capillaries in unchallenged synovium, with LYVE1⁺ macrophages absent from these aggregates (Fig. 5k). The number of these aggregates increased with age (Fig. 5l). We therefore hypothesized that they may arise in response to chronic circulating stimuli, including ICs, or those present in the context of inflammation/infection in distant organs. To test this, we challenged mice with i.v. IC twice over a period of 48 h (Fig. 5m). This resulted in the appearance of MHCII⁺ macrophage aggregates at 72 h (Fig. 5n,o). Furthermore, oral challenge with *Salmonella enterica* serovar Typhimurium, a colitogenic bacteria³¹, also induced synovial macrophage aggregates (Fig. 5p). However, chronic urinary tract infection with uropathogenic *Escherichia coli* did not induce macrophage aggregates in the synovium (Fig. 5q), suggesting that organ infection variably influences joints.

We next assessed the contribution of circulating monocytes to macrophage aggregate formation. A recent study³² established an in vivo protocol to fluorescently label intravascular leukocytes that were shielded from subsequent rounds of intravascular labeling once they entered tissues. We applied this system in our chronic IC stimulation model to assess the monocyte contribution to synovial macrophage aggregates. We administered i.v. ICs together with phycoerythrin (PE)-labeled anti-CD45 48 h before synovial collection, followed by administration of i.v. ICs and AF488-labeled anti-CD45 24 h before analysis (Extended Data Fig. 5a). Although we detected both 24- and 48-h time stamp signals in the spleen, synovial macrophage aggregates were not labeled with either 24- or 48-h time stamps (Extended Data Fig. 5b). Furthermore, using monocyte reporter *Ms4a3*^{Cre};*Rosa*^{tdT} mice, synovial macrophage aggregates were not labeled with tdTomato (Extended Data Fig. 5c), together indicating that these synovial macrophage clusters are derived from a local macrophage pool rather than circulating monocytes.

We next asked whether fibroblasts play any role as secondary effectors, responding to cues produced by FcγR-expressing synovial macrophages after IC challenge (Extended Data Fig. 6a). Bulk RNA-seq

of flow-sorted fibroblasts showed 417 IC-induced genes in synovial fibroblasts (Extended Data Fig. 6b,c), including *Cxcl1*, *Cxcl13* and *Ccl8* (Extended Data Fig. 6d). Enrichment analysis also showed that inflammatory response gene pathways, including interferon and IL-6–JAK–STAT3 signaling pathways, were upregulated following IC challenge (Extended Data Fig. 6e).

Together, these data show distinct responses of synovial macrophage subsets to circulating IC challenge, with LYVE1⁺CX₃CR1⁺ macrophages poised to trigger neutrophil recruitment but held in check by FcγRIIb expression. By contrast, CD11c⁺MHCII⁺ and CD11c⁺MHCII⁺ macrophages can present circulating antigens and respond to systemic immune stimuli, including ICs, by forming tight clusters around fenestrated capillaries, thus forming a physical barrier that might limit the spread of potentially harmful blood-borne cargo into the joint. In addition, synovial fibroblasts may function as secondary effectors, responding to macrophage cues.

Synovial macrophages activate nociceptors with IL-1β and nociceptors reciprocally enhance macrophage responses through CGRP

As joint pain is one of the most common features of systemic challenges, we next sought to determine the anatomical relationship between PVI⁺ capillaries and neurons. Sympathetic tyrosine hydroxylase⁺ (TH⁺) neurons primarily colocalized with αSMA⁺ arterioles in the sublining layer (Extended Data Fig. 7a), whereas calcitonin gene-related peptide⁺ (CGRP⁺) nociceptor neuronal fibers branched into the L–SL interface around PVI⁺ capillaries (Fig. 6a and Extended Data Fig. 7b). Quantification of the spatial location of macrophages, PVI⁺ vessels, PVI⁺ CD31⁺ vessels and CGRP⁺ fibers (Extended Data Fig. 8) indicated that approximately 30–40% of each macrophage subset were in direct contact with PVI⁺ vessels with LYVE1⁺CX₃CR1⁺ macrophages, and CD11c⁺ MNP preferentially localized to PVI⁺ vessels compared to PVI⁻ vessels (Fig. 6b). The average distance between CGRP⁺ fibers and macrophages was within 30 μm, and CD11c⁺ MNPs had the highest overlapped volume with CGRP⁺ fibers (Fig. 6c).

CGRP⁺ neuronal cell bodies were evident in the L4 dorsal root ganglia (DRG) that innervates the knee joint³³ (Extended Data Fig. 7c). Systemic IC injection induced activation of CGRP⁺ nociceptors in L4 but not T13 DRGs, as evidenced by neuronal pentraxin 2 (NP2) expression (Fig. 6d), an activity-dependent immediate early gene product³⁴ (Extended Data Fig. 9) that facilitates excitatory responses in peptidergic DRG neurons, including CGRP⁺ afferents³⁵. The proportion of CGRP⁺ neuronal bodies in the L4 DRGs did not change with IC injection nor anti-CSF1R treatment (Extended Data Fig. 7c,d).

Fig. 5 | Systemic IC challenge induces distinct responses in synovial macrophage subsets. **a**, Schematic diagram showing the protocol for bulk RNA-seq. **b**, Volcano plot showing DEGs due to OVA-IC stimulation in LYVE1⁺CX₃CR1⁺ macrophages from WT mice by RNA-seq; Sig., significantly. **c**, Venn diagram showing the number of common DEGs affected by IC stimulation between LYVE1⁺CX₃CR1⁺, MHCII⁺CD11c⁻ and MHCII⁺CD11c⁺ macrophages in WT and *Fcgr2b*^{-/-} mice. **d**, Gene ontology (GO) analysis of DEGs specific to each macrophage type with all the DEGs of three macrophage subsets as the background gene list; commun., communication; stim., stimulation; Pos, positive; O/E, observed/expected. **e**, Number of DEGs in each synovial macrophage from WT and *Fcgr2b*^{-/-} mice and common DEGs in both strains. **f**, Heat map of the expression of chemokines (scaled normalized values) with or without IC injection in LYVE1⁺CX₃CR1⁺ macrophages from WT and *Fcgr2b*^{-/-} mice. **g**, Ratio of mean *Cxcl1* expression in LYVE1⁺CX₃CR1⁺, MHCII⁺CD11c⁻ and MHCII⁺CD11c⁺ macrophages from WT and *Fcgr2b*^{-/-} mice injected i.v. with or without ICs; stim/unstim, stimulated/unstimulated. **h**, CXCL1 and CXCL2 enzyme-linked immunosorbent assay (ELISA) of the synovial digestion from *Fcgr2b*^{-/-} mice with or without IC injection; *n* = 5 (CXCL1) and 4 (CXCL2) mice for each group. **i**, Schematic diagram showing the protocol. **j**, Flow cytometry quantification of synovial neutrophils (Ly6G⁺ gates) from WT and *Fcgr2b*^{-/-} mice

injected i.v. with PBS, OVA or OVA;RaOVA 6 h before analysis; *n* = 3 (WT) and *n* = 6 (*Fcgr2b*^{-/-}) mice. **k**, Three-dimensional reconstruction of representative confocal images of whole-mount synovium depicting an MHCII⁺ macrophage cluster around PVI⁺ capillaries; scale bars, 200 (left), 50 (top right) and 100 μm (bottom right). Images are representative of at least two independent experiments with similar results. **l**, Number of MHCII⁺ macrophage clusters with a diameter of >30 μm in the whole-mount synovium in 4- and 52-week-old mice; *n* = 5 (4-week-old) and 6 (52-week-old) mice; w.o., weeks old; scale bars, 100 μm. **m**, Schematic diagram showing the protocol of systemic challenges. **n,o**, Number and images of MHCII⁺ macrophage clusters with a diameter of >30 μm in the whole-mount synovium in mice injected i.v. with PBS or OVA-IC over 2 consecutive days and analyzed 24 h after the last injection; *n* = 5 and 7 mice for each group. **p**, Number of MHCII⁺ macrophage clusters in mice infected orally with PBS or 5 × 10⁶ *S. enterica* serovar Typhimurium and analyzed after 3 weeks; *n* = 5 mice for each group; OG, oral gavage. The arrowheads in **l**, **o** and **p** mark macrophage clusters. **q**, Number of MHCII⁺ macrophage clusters in mice inoculated with two doses of 4 × 10⁷ uropathogenic *E. coli* into the bladder and analyzed after 3 weeks; *n* = 5 mice for each group. Data in **h**, **l** and **o–q** were analyzed by two-tailed *t*-test, data in **j** were analyzed by one-way ANOVA with Tukey's post hoc test, and data in **b** were analyzed by Wald test. Data are shown as mean ± s.e.m. in **h**, **j**, **l** and **n–q**.

Because neurons do not express FcγRs and are therefore incapable of direct detection of circulating ICs, we hypothesized that adjacent FcγR-expressing macrophages relay their presence and activate CGRP⁺ nociceptors. To test this, we used anti-CSF1R that preferentially depleted LYVE1⁺ macrophages (Fig. 6e and Extended Data Fig. 7e,f). This attenuated the activation of CGRP⁺ nociceptors (Fig. 6f), confirming potential cross-talk between macrophages and CGRP⁺ nociceptors. Because anti-CSF1R potentially depletes macrophages in other tissues, we added supernatants from synovial whole-mount explants stimulated with OVA or IC to DRG neurons to validate a specific effect of synovial macrophages ex vivo (Fig. 6g). This induced the release of CGRP from DRG neurons, an effect absent in IC-stimulated synovium dissected from anti-CSF1R-treated mice (Fig. 6h). We next used our bulk RNA-seq data from IC-stimulated LYVE1⁺CX₃CR1⁺ macrophages to prioritize inhibitors for testing in our ex vivo DRG culture model. This analysis identified several candidate molecules upregulated in IC-stimulated macrophages that have previously been described to mediate immune cell interactions with neurons^{17,36}, including *Cxcl1*, *Tnf* and *Il1β* (Fig. 6i), and neutralization of IL-1β partly suppressed the excitation of DRG neurons (Fig. 6j and Extended Data Fig. 10a). Because *Cx3cr1*^{CreER} mice label lining macrophages in naive animals^{7,24}, we crossed *Cx3cr1*^{CreER} mice with *Il-1β*^{fl/fl} mice to ablate IL-1β in LYVE1⁺CX₃CR1⁺ macrophages. Cre recombinase activation of *Cx3cr1*^{CreER}*Il-1β*^{fl/fl} mice resulted in a marked reduction of IL-1β production in the synovium (Fig. 6k), and we observed a reduction in nociceptor activation in L4 DRGs but not in nonjoint innervating T13 DRGs, demonstrating a role for synovial lining macrophage-derived IL-1β in activating nociceptor neurons (Fig. 6l).

Finally, we asked whether cross-talk between immune cells and nociceptor neurons in the synovium may also involve reciprocal signals from neurons to macrophages. scRNA-seq data of healthy synovium⁶ showed that *Ramp1*, *Ramp2* and *Calcrl* were the most highly expressed among neuropeptide receptor transcripts and *Ramp1*, which forms a complex with calcitonin receptor-like receptor to form the CGRP receptor, was particularly expressed in MHCII⁺ macrophages (Fig. 7a and Extended Data Fig. 10b,c). Bulk RNA-seq data confirmed *Ramp1* expression in MHCII⁺ macrophages, particularly the CD11c⁺ population (Fig. 7b). To investigate the functional importance of CGRP receptor expression in MHCII⁺ synovial macrophages, we stimulated whole synovial explants with CGRP for 4 h and sorted both MHCII⁺ macrophage subsets for bulk RNA-seq (Fig. 7c). We observed robust transcriptional responses to CGRP stimulation (Extended Data Fig. 10d), with some genes increased in both subsets, but almost half of the DEGs were unique to each macrophage subset (Fig. 7d and Extended Data Fig. 10e).

Fig. 6 | Synovial macrophages activate nociceptors in part through IL-1β.

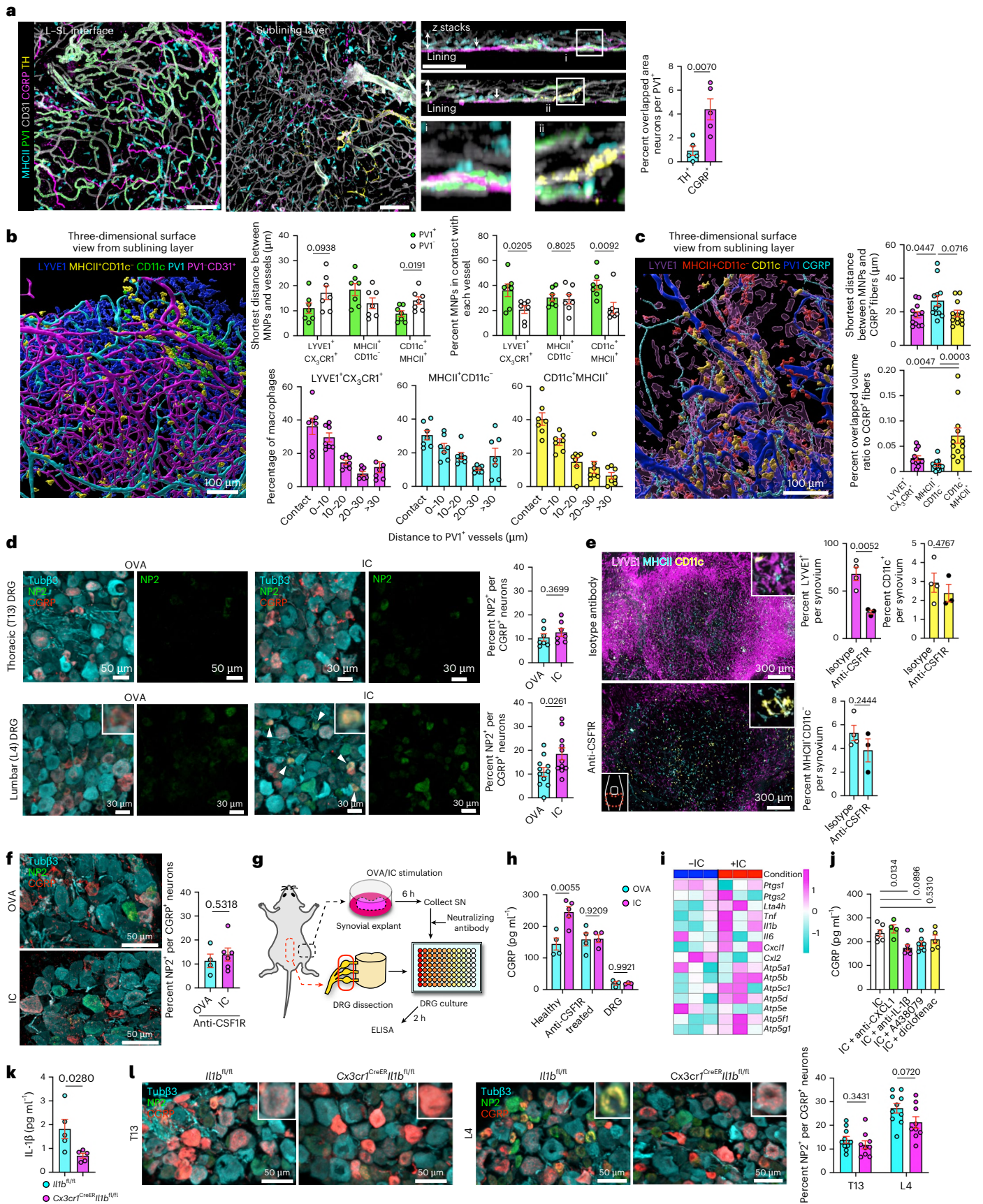
a, Three-dimensional reconstruction of representative confocal images of whole-mount synovium; scale bars, 100 μm. Arrows indicate CGRP⁺ neurons in z-stack images; *n* = 5 mice for each group. **b**, Three-dimensional reconstruction of representative confocal images of whole-mount synovium using the Surface module in Imaris and quantification of the distance between each macrophage subset and vessels; *n* = 7 mice for each group. Each plot indicates the mean value of each mouse. **c**, Three-dimensional reconstruction of representative confocal images of whole-mount synovium using the Surface module in Imaris and quantification of the distance or overlapped volume ratio between each macrophage subset and CGRP⁺ fibers; *n* = 12 mice for each group. Each plot indicates the mean value of each mouse. **d**, Representative confocal images of lumbar (L4) and thoracic (T13) DRG in mice injected i.v. with OVA or OVA-IC and analyzed after 6 h; *n* = 7 (T13) and 11 (L4) mice for each group; Tubβ3, tubulin-β3. The arrowheads indicate the merged area for NP2 and CGRP. **e**, Three-dimensional reconstruction of representative confocal images of whole-mount synovium from mice injected intraperitoneally (i.p.) with 400 μg of anti-CSF1R or isotype control antibody and analyzed after 72 h. Quantification of the percentage of area covered by each macrophage subset in the synovium is shown on the right; *n* = 4 (isotype) and 3 (anti-CSF1R) mice. **f**, Representative confocal images of L4 DRG in mice injected i.v. with OVA or OVA-IC 72 h after i.p. injection with 400 μg of anti-CSF1R; *n* = 4 (OVA) and 6 (IC) mice. **g**, Illustration

of experimental protocol; SN, supernatant. **h**, CGRP ELISA of DRG culture SN stimulated with SN from OVA- or IC-stimulated synovial explants from indicated mice or directly stimulated with OVA or IC; *n* = 3 to 5 mice for each group. **i**, Heat map of the expression of potential candidates responsible for immune-driven pain in bulk RNA-seq data from IC-stimulated LYVE1⁺CX₃CR1⁺ macrophages (scaled normalized values). **j**, CGRP ELISA of DRG culture supernatants stimulated with supernatants from IC-stimulated synovial explants. Indicated neutralizing antibodies (4 μg ml⁻¹) or A438079 (100 μM) was added to synovial SN before adding to DRG neurons. Diflofenac (200 μM) was added with IC when stimulating synovial explants; *n* = 6 (IC), 4 (CXCL1), 7 (IL-1β), 7 (A438079) and 5 (Coxi) mice. **k**, IL-1β concentration of the synovial digestion measured by cytometric bead array from *Il1b*^{fl/fl} and *Cx3cr1*^{CreER}*Il1b*^{fl/fl} mice 12 h after i.p. injection of 2 mg per kg (body weight) lipopolysaccharide (LPS); *n* = 5 mice for each group. **l**, Representative confocal images of T13 and L4 DRG in *Il1b*^{fl/fl} and *Cx3cr1*^{CreER}*Il1b*^{fl/fl} mice injected i.v. with OVA-IC. Mice were i.p. injected with tamoxifen twice 48 h apart 2 weeks before IC injection and analyzed 6 h after IC injection; *n* = 10 (*Il1b*^{fl/fl}) and 9 (*Cx3cr1*^{CreER}*Il1b*^{fl/fl}) mice. Data in **a**, **b**, **d**–**f**, **h**, **k** and **l** were analyzed by two-tailed *t*-test. The IC group was used as a control group in a one-way ANOVA with Dunnett's post hoc test in **j**. Data in **c** were analyzed by one-way ANOVA with Tukey's post hoc test. Data in **a**–**f**, **h** and **j**–**l** represent mean ± s.e.m.

Discussion

Joint pain or inflammation is a common and early feature of several systemic diseases. These include autoimmune diseases, such as systemic lupus erythematosus, adult onset Still's disease and inflammatory bowel disease, as well as infection in organs distant to the musculoskeletal system, including enteric or genitourinary infections, streptococcal pharyngitis and viral infections, for example, parvovirus^{2–4}. The pathogenic mediators vary, but circulating ICs or microbial antigens have been implicated³⁷. However, why joints are highly responsive to systemic inflammation is unknown. We sought to address this question, developing a whole-mount imaging system of the entire synovium to profile the vascular, neuronal and immune components. This revealed that highly permeable PVI⁺ capillaries were specifically located at the L–SL interface in the periphery of the synovium, enabling entry of circulating stimuli into the joint. We found that this area of vulnerability was occupied by three subsets of macrophages that demonstrated distinct responses to systemic IC challenge and interacted with nociceptor neurons, forming a blood–joint barrier (BJB) to defend joint tissue.

The location of fenestrated capillaries and their defensive macrophage–nociceptor sentinel unit in the periphery of the synovium at the synovia–bone interface is particularly interesting because this is the site of onset and formation of destructive granulomatous pannus in RA^{13,15}. RA is characterized by circulating antibodies, including rheumatoid factor (IgM antibodies specific for the Fc portion of IgG) and anti-citrullinated protein IgG¹. Our study identifies a fenestrated capillary bed that would enable access of autoantibodies or IC to the synovium at the very site of pannus formation. We found that adjacent macrophages expressed FcγRs, enabling responses to circulating IC and autoantibodies that might access the synovium via the fenestrated vasculature. Indeed, the inhibitory receptor FcγRIIb was a critical



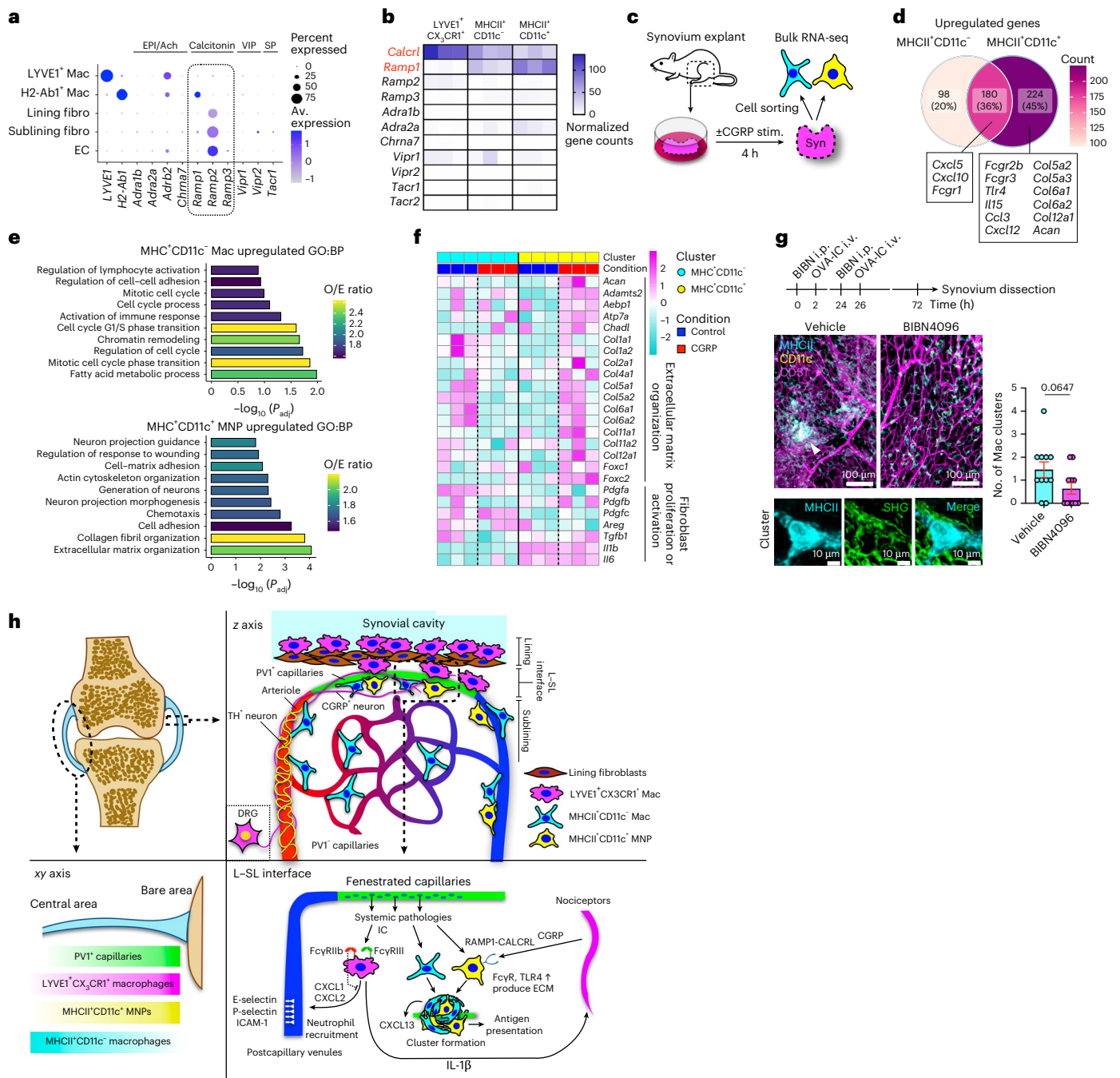


Fig. 7 | Nociceptors reciprocally enhance synovial macrophage responses through CGRP. **a**, Dot plots showing the average expression levels and the percentage of cells from each cluster expressing genes for neuropeptide receptors. scRNA-seq data are from GSE145286; EPI, epinephrine; Ach, acetylcholine; VIP, vasoactive intestinal polypeptide; SP, substance P; EC, endothelial cell; fibro, fibroblast; Av., average. **b**, Heat map of expression of genes for neuropeptide receptors in LYVE1⁺CX₃CR1⁺, MHCII⁺CD11c⁻ and MHCII⁺CD11c⁺ macrophages from bulk RNA-seq analysis (normalized values). *Ramp1* and *Calcr1*, which encode proteins that form the CGRP receptor complex, are highlighted in red font. **c**, Illustration of the experimental protocol for bulk RNA-seq analysis. **d**, Venn diagram showing the number of distinct and common DEGs affected by CGRP stimulation between MHCII⁺CD11c⁻ and MHCII⁺CD11c⁺ macrophages. **e**, Gene ontology (GO) analysis of DEGs specific to each macrophage type with

all the DEGs of two macrophage subsets as the background gene list. Fisher's exact test was used; BP, biological process. **f**, Heat map of expression of genes related to extracellular matrix organization and fibroblast proliferation with CGRP stimulation in MHCII⁺CD11c⁻ and MHCII⁺CD11c⁺ macrophages (scaled normalized values). The vertical dashed lines mark the border of control and CGRP groups. **g**, Number of MHCII⁺ macrophage clusters with a diameter of >30 μm and second harmonic generation (SHG) on the clusters in the whole-mount synovium in mice injected i.v. with OVA-IC over 2 consecutive days after treatment with BIBN4096 (BIBN; 500 μg per kg (body weight) i.p.) or vehicle; *n* = 11 mice for each group. Data are shown as mean ± s.e.m. and were analyzed by two-tailed *t*-test. **h**, Schematic diagram of the immune-histochemical microarchitecture of the entire synovium and the sentinel unit surrounding PV1⁺ capillaries; ECM, extracellular matrix.

regulator of IC-induced activation of LYVE1⁺CX₃CR1⁺ macrophages, with neutrophil recruitment to the synovium evident in its absence. Our data are consistent with human studies in RA showing that individuals with an *FCGR2B* polymorphism associated with receptor dysfunction demonstrate increased joint damage³⁸.

The presence of highly permeable PVI⁺ capillaries in the synovium provides a mechanistic explanation for the joint manifestations of infections affecting organs distal to the musculoskeletal system. Previous studies have identified the presence of bacterial rRNA in a wide spectrum of inflammatory joints³⁹ and viral nucleic acids in viral-associated arthritis⁴⁰. Together, this suggests that the synovium is accessible to circulating microbes or microbial components. Clinically, reactive arthritis is characterized by a neutrophil-rich synovial effusion⁴¹, consistent with our observation that PVI⁺ capillary-associated synovial macrophages avidly produce neutrophil-recruiting chemokines in response to circulating stimuli. In addition, we found that *S. enterica* serovar Typhimurium colitis promoted macrophage cluster formation around PVI⁺ capillaries in the synovium, potentially reflecting the pathology of reactive arthritis.

Using the *Ms4a3^{Cre}-Rosa^{Tdt}* model, we assessed the contribution of circulating monocytes to synovial macrophages under steady-state conditions. Compared to other organs that have no monocyte contribution (microglia, Kupffer cells and Langerhans cells), fast replacement (gut and dermis) or slow replacement (kidney and spleen)²⁸, synovial macrophages have heterogeneous kinetics, with the MHCII⁺ macrophage pool having a greater monocyte contribution than LYVE1⁺CX₃CR1⁺ lining macrophages. Whole-mount synovial imaging also showed that monocytes preferentially replace synovial macrophages in the synovia–bone interface where proliferative pannus arises in RA, which further highlights the importance of PVI⁺ fenestrated capillaries as sites where joint pathology is initiated.

The activation of nociceptors alerts humans to the presence of harmful stimuli, leading to pain⁴². There has been recent interest in potential interactions between nociceptors and immune cells, including via neuropeptides, mainly in the context of infectious diseases where bacteria or fungi can directly activate nociceptors^{16,43–45}. By contrast, our study shows that synovial macrophages sense local IC challenge and stimulate nociceptors, an effect mediated in part through IL-1 β . IL-1 β has also been previously implicated in augmenting pain sensitivity by promoting prostaglandin production⁴⁶, upregulating transient receptor potential cation channel subfamily V member 1 (ref. 47) and generating action potentials in a p38 MAP kinase-dependent manner⁴⁸. Our results suggest that IL-1 receptor antagonists may be a useful therapy for joint pain in a variety of IC-mediated diseases. Other candidates responsible for immune-driven joint pain should be explored in future studies. Furthermore, we found that this immune-driven nociceptor activation led to CGRP production, which in turn affected CD11c⁺MHCII⁺ MNP, increasing the expression of IC and pathogen-associated molecular pattern receptors, such as *Fcgr2b*, *Fcgr3* and *Tlr4*. This heightened ability to detect and be activated by circulating stimuli reinforces a physical barrier to defend the area of vulnerability around PVI⁺ capillaries. Among the interstitial macrophages, CD11c⁺MHCII⁺ macrophages and CD11c⁺MHCII⁺ MNPs showed distinct spatial localization (Fig. 2f), transcriptional profiles in the homeostatic state (Fig. 3b) and responses to IC and CGRP stimulation (Figs. 5c and 7d–f).

Finally, perhaps the most interesting question is why a BJB equipped to sense circulating stimuli and telegraph their presence via pain has evolved. It is tempting to speculate that there might be a selective advantage to such a warning system at both an individual and species level. First, arthralgia might reduce mobility and thereby preserve energy for immune responses. Second, reduced movement may limit the transmission of infectious diseases to other individuals. Similar concepts have been proposed to explain why some infection-associated cytokines lead to increased anxiety and reduced socialization⁴⁹.

Together, our data show how the unique anatomical arrangement of cells in the peripheral region of the synovium provides access to circulating immune stimuli through fenestrated capillaries and how this is policed by interacting macrophages and nociceptor neurons. Our findings have implications for the development of treatment strategies for immune-driven arthralgia.

Online content

Any methods, additional references, Nature Portfolio reporting summaries, source data, extended data, supplementary information, acknowledgements, peer review information; details of author contributions and competing interests; and statements of data and code availability are available at <https://doi.org/10.1038/s41590-024-02011-8>.

References

- Smolen, J. S., Aletaha, D. & McInnes, I. B. Rheumatoid arthritis. *Lancet* **388**, 2023–2038 (2016).
- García-Kutzbach, A., Chacón-Súchite, J., García-Ferrer, H. & Iraheta, I. Reactive arthritis: update 2018. *Clin. Rheumatol.* **37**, 869–874 (2018).
- Mackie, S. L. & Keat, A. Poststreptococcal reactive arthritis: what is it and how do we know? *Rheumatology* **43**, 949–954 (2004).
- Franssila, R. & Hedman, K. Viral causes of arthritis. *Best. Pract. Res. Clin. Rheumatol.* **20**, 1139–1157 (2006).
- Ceccarelli, F. et al. Joint involvement in systemic lupus erythematosus: from pathogenesis to clinical assessment. *Semin. Arthritis Rheum.* **47**, 53–64 (2017).
- Wei, K. et al. Notch signalling drives synovial fibroblast identity and arthritis pathology. *Nature* **582**, 259–264 (2020).
- Culemann, S. et al. Locally renewing resident synovial macrophages provide a protective barrier for the joint. *Nature* **572**, 670–675 (2019).
- Simkin, P. A. The human knee: a window on the microvasculature. *Tissue Barriers* **3**, e970465 (2015).
- Simkin, P. A. & Bassett, J. E. Pathways of microvascular permeability in the synovium of normal and diseased human knees. *J. Rheumatol.* **38**, 2635–2642 (2011).
- Knight, A. D. & Levick, J. R. Effect of fluid pressure on the hydraulic conductance of interstitium and fenestrated endothelium in rabbit knee. *J. Physiol.* **360**, 311–332 (1985).
- Mapp, P. I. Innervation of the synovium. *Ann. Rheum. Dis.* **54**, 398–403 (1995).
- Smith, M. D. The normal synovium. *Open Rheumatol. J.* **5**, 100–106 (2012).
- Schett, G. & Gravallese, E. Bone erosion in rheumatoid arthritis: mechanisms, diagnosis and treatment. *Nat. Rev. Rheumatol.* **8**, 656–664 (2012).
- Hasegawa, T., Kikuta, J. & Ishii, M. Imaging of bone and joints in vivo: pathological osteoclastogenesis in arthritis. *Int. Immunol.* **33**, 679–686 (2021).
- Hasegawa, T. et al. Identification of a novel arthritis-associated osteoclast precursor macrophage regulated by FoxM1. *Nat. Immunol.* **20**, 1631–1643 (2019).
- Pinho-Ribeiro, F. A. et al. Bacteria hijack a meningeal neuroimmune axis to facilitate brain invasion. *Nature* **615**, 472–481 (2023).
- Baral, P., Udit, S. & Chiu, I. M. Pain and immunity: implications for host defence. *Nat. Rev. Immunol.* **19**, 433–447 (2019).
- Straub, R. H. & Pongratz, G. Role of peripheral nerve fibres in acute and chronic inflammation in arthritis. *Nat. Rev. Rheumatol.* **9**, 117–126 (2013).
- Thiriot, A. et al. Differential DARC/ACKR1 expression distinguishes venular from non-venular endothelial cells in murine tissues. *BMC Biol.* **15**, 45 (2017).

20. Stan, R. V. et al. The diaphragms of fenestrated endothelia: gatekeepers of vascular permeability and blood composition. *Dev. Cell* **23**, 1203–1218 (2012).
21. Carloni, S. et al. Closing during intestinal inflammation. *Science* **448**, 439–448 (2021).
22. Lee, D. et al. Cadherin-11 in synovial lining formation and pathology in arthritis. *Science* **315**, 1006–1010 (2007).
23. Croft, A. P. et al. Distinct fibroblast subsets drive inflammation and damage in arthritis. *Nature* **570**, 246–251 (2019).
24. Zec, K. et al. Macrophages in the synovial lining niche initiate neutrophil recruitment and articular inflammation. *J. Exp. Med.* **220**, e20220595 (2023).
25. Radtke, A. J. et al. IBEX: a versatile multiplex optical imaging approach for deep phenotyping and spatial analysis of cells in complex tissues. *Proc. Natl Acad. Sci. USA* **117**, 33455–33465 (2020).
26. Clatworthy, M. R. et al. Immune complexes stimulate CCR7-dependent dendritic cell migration to lymph nodes. *Nat. Med.* **20**, 1458–1463 (2014).
27. Xue, J. et al. Transcriptome-based network analysis reveals a spectrum model of human macrophage activation. *Immunity* **40**, 274–288 (2014).
28. Liu, Z. et al. Fate mapping via MS4A3—expression history traces monocyte-derived cells. *Cell* **178**, 1509–1525 (2019).
29. Smith, K. G. C. & Clatworthy, M. R. FcγRIIB in autoimmunity and infection: evolutionary and therapeutic implications. *Nat. Rev. Immunol.* **10**, 328–343 (2010).
30. Li, W., Germain, R. N. & Gerner, M. Y. High-dimensional cell-level analysis of tissues with Ce3D multiplex volume imaging. *Nat. Protoc.* **14**, 1708–1733 (2019).
31. Hapfelmeier, S. & Hardt, W. D. A mouse model for *S. typhimurium*-induced enterocolitis. *Trends Microbiol.* **13**, 497–503 (2005).
32. Kirschenbaum, D. et al. Time-resolved single-cell transcriptomics defines immune trajectories in glioblastoma. *Cell* **187**, 149–165 (2024).
33. Aso, K. et al. Nociceptive phenotype of dorsal root ganglia neurons innervating the subchondral bone in rat knee joints. *Eur. J. Pain* **18**, 174–181 (2014).
34. O'Brien, R. J. et al. Synaptic clustering of AMPA receptors by the extracellular immediate-early gene product *Narp*. *Neuron* **23**, 309–323 (1999).
35. Kanehisa, K. et al. Neuronal pentraxin 2 is required for facilitating excitatory synaptic inputs onto spinal neurons involved in pruriceptive transmission in a model of chronic itch. *Nat. Commun.* **13**, 2367 (2022).
36. Hasebe, R. et al. ATP spreads inflammation to other limbs through crosstalk between sensory neurons and interneurons. *J. Exp. Med.* **219**, e20212019 (2022).
37. Toivanen, P. & Toivanen, A. Two forms of reactive arthritis? *Ann. Rheum. Dis.* **58**, 737–741 (1999).
38. Radstake, T. R. D. J. et al. The functional variant of the inhibitory Fcγ receptor IIb (CD32B) is associated with the rate of radiologic joint damage and dendritic cell function in rheumatoid arthritis. *Arthritis Rheum.* **54**, 3828–3837 (2006).
39. Kempell, K. E. et al. Reverse transcriptase-PCR analysis of bacterial rRNA for detection and characterization of bacterial species in arthritis synovial tissue. *Infect. Immun.* **68**, 6012–6026 (2000).
40. Moore, T. Parvovirus-associated arthritis. *Curr. Opin. Rheumatol.* **12**, 289–294 (2000).
41. Hønge, B. L., Hermansen, M. L. F. & Storgaard, M. Reactive arthritis after COVID-19. *BMJ Case Rep.* **14**, 2020–2022 (2021).
42. Basbaum, A. I., Bautista, D. M., Scherrer, G. & Julius, D. Cellular and molecular mechanisms of pain. *Cell* **139**, 267–284 (2009).
43. Cohen, J. A. et al. Cutaneous TRPV1⁺ neurons trigger protective innate type 17 anticipatory immunity. *Cell* **178**, 919–932 (2019).
44. Chiu, I. M. et al. Bacteria activate sensory neurons that modulate pain and inflammation. *Nature* **501**, 52–57 (2013).
45. Maruyama, K. et al. Nociceptors boost the resolution of fungal osteoinflammation via the TRP channel-CGRP-JDP2 axis. *Cell Rep.* **19**, 2730–2742 (2017).
46. Cunha, T. M. et al. A cascade of cytokines mediates mechanical inflammatory hypernociception in mice. *Proc. Natl Acad. Sci. USA* **102**, 1755–1760 (2005).
47. Ebbinghaus, M. et al. The role of interleukin-1β in arthritic pain: main involvement in thermal, but not mechanical, hyperalgesia in rat antigen-induced arthritis. *Arthritis Rheum.* **64**, 3897–3907 (2012).
48. Binshtok, A. M. et al. Nociceptors are interleukin-1β sensors. *J. Neurosci.* **28**, 14062–14073 (2008).
49. Filiano, A. J. et al. Unexpected role of interferon-γ 3 in regulating neuronal connectivity and social behaviour. *Nature* **535**, 425–429 (2016).

Publisher's note Springer Nature remains neutral with regard to jurisdictional claims in published maps and institutional affiliations.

Open Access This article is licensed under a Creative Commons Attribution 4.0 International License, which permits use, sharing, adaptation, distribution and reproduction in any medium or format, as long as you give appropriate credit to the original author(s) and the source, provide a link to the Creative Commons licence, and indicate if changes were made. The images or other third party material in this article are included in the article's Creative Commons licence, unless indicated otherwise in a credit line to the material. If material is not included in the article's Creative Commons licence and your intended use is not permitted by statutory regulation or exceeds the permitted use, you will need to obtain permission directly from the copyright holder. To view a copy of this licence, visit <http://creativecommons.org/licenses/by/4.0/>.

© The Author(s) 2024

¹Molecular Immunity Unit, University of Cambridge, Department of Medicine, Medical Research Council Laboratory of Molecular Biology, Cambridge, UK. ²Cambridge Institute for Therapeutic Immunology and Infectious Diseases, University of Cambridge, Cambridge, UK.

³Cellular Genetics, Wellcome Sanger Institute, Hinxton, UK. ⁴Division of Trauma and Orthopaedic Surgery, Department of Surgery, University of Cambridge, Cambridge, UK. ⁵Department of Physiology, Keio University School of Medicine, Tokyo, Japan. ⁶Department of Anatomy, Faculty of Medicine, Hokkaido University, Sapporo, Japan. ⁷Momentum Laboratory of Neuroimmunology, Institute of Experimental Medicine, Budapest, Hungary.

⁸Shanghai Institute of Immunology, Shanghai Jiao Tong University School of Medicine, Shanghai, China. ⁹INSERM U1015, Gustave Roussy, Villejuif, France.

✉ e-mail: th647@cam.ac.uk; mrc38@medschl.cam.ac.uk

Methods

Mice

WT mice (C57BL/6J background) were bred in-house or purchased from The Jackson Laboratory. Transgenic mice expressing Venus enhanced yellow fluorescent protein under the control of the *Itgax* promoter were a gift from M. Nussenzweig (Rockefeller University). *Fcgr2b*^{-/-} mice were kindly provided by J. Ravetch (Rockefeller University) and S. Bolland (US National Institutes of Health and US National Institute of Allergy and Infectious Diseases)⁵⁰. *Il1b*^{fl/fl} floxed mice were crossed with tamoxifen-inducible B6.129P2(C)-*Cx3cr1*^{tm2.1(cre/ERT2)ung/l} mice (The Jackson Laboratory, 020940) as described before⁵¹. Cre recombinase activity was induced by two i.p. injections of tamoxifen (2 mg 100 μ l⁻¹, Sigma-Aldrich, dissolved in corn oil) 48 h apart in 5- to 7-week-old male mice 2 weeks before the experiment.

In all experiments, both male and female mice were used. For all in vivo experiments, 8- to 20-week-old mice were used unless otherwise mentioned. Mice were maintained under specific pathogen-free conditions at a Home Office-approved facility with controlled humidity and temperature with a 12-h light/12-h dark cycle in the United Kingdom. All procedures were ethically approved by the University of Cambridge Animal Welfare and Ethical Review Body and were performed in accordance with the United Kingdom Animals (Scientific Procedures) Act of 1986 under the authority of a UK Home Office Licence.

Human samples

Human synovial specimens were obtained from individuals with osteoarthritis undergoing replacement surgery or synovectomy with prior ethical approval (18/NW/0545) and informed consent at Addenbrooke's Hospital, Cambridge. Samples were obtained from two male and three female donors aged 57–83. Participant compensation was not applicable.

Generation and administration of small circulating ICs

All compounds were administered i.v. via tail vein injection using a 30-G insulin syringe (Becton Dickinson). ICs were prepared in vitro by incubating AF647-OVA (2 mg ml⁻¹ in PBS; Invitrogen, O34784) with rabbit polyclonal anti-OVA antiserum (3.7 mg ml⁻¹; Sigma-Aldrich, C-6534) at a 1:1 molar ratio (40 μ g of OVA + 150 μ g of RaOVA) for 60 min in a 37 °C water bath²⁶.

Infectious models

Mice were infected orally with approximately 5×10^6 colony-forming units of *S. enterica* serovar Typhimurium (stain BRD509). Twenty-four hours before infection, mice were gavaged with 20 mg of streptomycin (Bio Basic, SBO494) in 100 μ l of PBS to aid colonization. Colony-forming unit counts were verified by streaking the inoculums on to agar plates postgavage. Mice were culled 21 days later by rising CO₂ concentration.

Urinary tract infection was induced in experimental mice as previously described⁵². Briefly, under isoflurane anesthesia (Baxter), the perineum was cleaned with ethanol, and the urethra was catheterized using 0.28 \times 0.60 mm polyethylene tubing (Instech Laboratories) lubricated in sterile Instillagel (CliniMed). In total, 4×10^7 colony-forming units in 100 μ l of prepared uropathogenic *E. coli* (strain UTI89) were inoculated into the bladder during one session. Repeated inoculation was performed with 2-h intervals to increase the likelihood of ascending pyelonephritis. Mice were culled 21 days later by rising CO₂ concentration.

Isolation of synovium leukocytes from tissues

After death by anesthesia, the right auricles of the mice were cut, and 10 ml of prewarmed 1 \times PBS was injected into the left ventricle for perfusion. Perfusion was omitted in experiments designed to assess blood samples.

After removal of the skin, the quadriceps femoris muscles were carefully removed. Attachment of the synovium to the bare area of

femur was observed by pinching and lifting up the patella with tweezers under a stereoscopic microscope (Stemi 2000-CS, Zeiss). The bone-synovium and meniscus-synovium interface was carefully dissected throughout the knee joint without damaging the bone, and the patella was removed at the end. For flow cytometry analysis, whole-mount synovial tissues were digested with 2 mg ml⁻¹ type I collagenase in RPMI and incubated at 37 °C for 45 min. Disaggregated tissue elements were passed through a 70- μ m cell strainer.

Flow cytometry

Measurements were performed on an CytoFLEX LX (Beckman Coulter) and analyzed with FlowJo software (Tree Star). Sorting was performed on an FACS Aria Fusion (Becton Dickinson). Single-cell suspensions were incubated with Zombie Aqua (Biolegend) or Viakrome 808 fixable viability dye (Beckman Coulter) diluted 1:250 in PBS for 15 min at 4 °C. Samples were centrifuged and resuspended in FACS buffer supplemented with anti-CD16/CD32 (Biolegend) diluted 1:50, followed by staining with antibodies for 15 min at 4 °C. Antibodies used in this study are listed in Supplementary Table 1.

Confocal and multiphoton microscopy of mouse samples

Dissected knee joints were fixed in fixative solution made with 9% Glyoxal (Sigma-Aldrich, 128465) and 40% Antigenfix (Diapath, P0016) overnight at 4 °C. For sagittal section imaging, samples were decalcified in 14% EDTA solution for 12 days, followed by 4 h in 30% sucrose in PBS. EDTA was replaced every 72 h. Then, 30- μ m sections were blocked and permeabilized in 0.1 M Tris containing 0.3% Triton X-100 (MilliporeSigma), 1% normal mouse serum, 1% normal donkey serum and 1% bovine serum albumin (BSA; R&D Systems). Samples were stained for 2 h at room temperature (RT) in a wet chamber with the appropriate antibodies, washed three times in PBS and mounted in Fluoromount-G (Southern Biotech). For whole-mount imaging, the knee synovium was dissected, as described above, and blocked and permeabilized in 0.1 M Tris containing 0.1% Triton X-100, 1% normal mouse serum, 1% normal donkey serum and 1% BSA in 0.5-ml Eppendorf safe-lock tubes. Samples were stained for 12 h at 4 °C with the appropriate antibodies in 0.5-ml Eppendorf safe-lock tubes, washed three times extensively in PBS and mounted in Fluoromount-G. Images were acquired using a TCS SP8 inverted confocal microscope with a scan format of 512 \times 512 (Leica Microsystems) or TCS SP8 3X gated STED confocal inverted microscope (Leica Microsystems) with a \times 40/1.3-NA oil or \times 40/1.1-NA water objective. Second harmonic generation images were acquired using a Zeiss 710 NLO upright multiphoton microscope equipped with a \times 20 water objective and infrared lasers (880 nm) driven by a Ti sapphire laser. Raw imaging data were processed, and a Gaussian filter was applied using Imaris (Bitplane). The antibodies used in this study are listed in Supplementary Table 1.

Confocal microscopy of human samples

Human synovial specimens were fixed in a fixative solution made with 9% Glyoxal (Sigma-Aldrich, 128465) and 40% Antigenfix (Diapath, P0016) at 4 °C. For sagittal section imaging, samples were placed in 30% sucrose in PBS for 4 h and embedded in OCT embedding matrix (CellPath). Sections were incubated with primary antibodies for 2 h at RT and washed three times in PBS. Sections were then incubated with the appropriate fluorochrome-labeled secondary antibodies for 1 h at RT, washed in PBS and mounted in Fluoromount-G. For whole-mount imaging, synovium samples were dissected into 1 \times 1 cm pieces and blocked and permeabilized in 0.1 M Tris containing 0.3% Triton X-100, 1% normal donkey serum, 1% BSA and 0.1% saponin (Sigma). Samples were incubated with primary antibodies for 12 h at 4 °C and washed three times extensively in PBS. Samples were then incubated with the appropriate fluorochrome-labeled secondary antibodies for 12 h at 4 °C and washed three times in PBS. Samples were then embedded in Ce3D solution³⁰ for 12 h to clear the tissue and mounted in Ce3D solution.

Images were acquired using a TCS SP8 inverted confocal microscope or TCS SP8 3X gated STED confocal inverted microscope on a $\times 40/1.3$ -NA oil or $\times 40/1.1$ -NA water objective. Raw imaging data were processed, and a Gaussian filter was applied using Imaris (Bitplane). Antibodies used in this study are listed in Supplementary Table 1.

Iterative staining

Iterative staining of sections was performed as previously described^{25,53}. Following acquisition of initial images, the coverslip was removed, and slides were washed three times in PBS to remove mounting medium. Bleaching of the fluorochromes was achieved using a 1 mg ml^{-1} solution of lithium borohydride in water (Acros Organics) for 15 min at RT. The slides or whole-mount synovium were washed three times in PBS before staining with a different set of antibodies. The process was repeated up to three times. Raw imaging data were processed using Imaris (Bitplane), and Hoechst or CD31 was used as fiducial for the alignment of subsequent images.

Dissection and culture of mouse DRG neurons

DRG neurons were bilaterally excised under a dissection microscope as previously described⁵⁴. For section images, lumbar (L4) or thoracic (T13) DRGs were embedded in OCT embedding matrix, and sections were subsequently made. For culture systems, DRGs were digested with the combined 1.25 mg ml^{-1} collagenase A + 2.5 mg ml^{-1} Dispase II solution for 30 min at 37°C . Sensory neurons were cultured on laminin-coated 96-well plates in Neurobasal medium (Thermo Fisher Scientific) supplemented with 1% GlutaMAX (Thermo Fisher Scientific), 50 ng ml^{-1} NGF 2.5S (Gibco) and B-27 supplement (Gibco) for 36 h to remove glial and axon debris that float in the medium. For CGRP release assays, ICs were prepared in vitro by incubating OVA with rabbit polyclonal anti-OVA ($1 \mu\text{g}$ of OVA + $18.5 \mu\text{g}$ of RaOVA) for 30 min in a 37°C water bath, spinning down the pellet and washing with PBS three times. Synovium explants were stimulated with OVA or ICs in $200 \mu\text{l}$ of RPMI for 6 h, and DRG neurons were incubated with the supernatants for 2 h at 37°C and 5% CO_2 . After incubation, the DRG supernatant was collected and used to quantify the concentration of CGRP using an ELISA kit (Antibodies.com) according to the manufacturer's instructions.

CGRP stimulation assay from synovium explants

Whole-mount synovium was dissected from WT mice and incubated with CGRP (100 nM) or vehicle for 4 h. After incubation, the synovium was digested as described above, and macrophages were sorted into $350 \mu\text{l}$ of Buffer RLT Plus (Qiagen) using a FACS Aria Fusion (Becton Dickinson).

In vivo BIBN4096 treatment

The impact of CGRP signaling on the outcome of systemic IC challenge was evaluated by treating mice with the RAMP1 antagonist BIBN4096 (Tocris), as described previously¹⁶. Mice were treated by i.p. injection of BIBN4096 (0.5 mg per kg (body weight)) or vehicle 2 h before i.v. IC injection for 2 d in a row, and knee synovium was dissected 48 h after the last injection.

Cytometric bead array

Concentrations of IL-1 β were determined by BD Cytometric Bead Array using the Mouse IL-1 β Enhanced Sensitivity Flex Set (562278) according to the manufacturer's instructions. Bilateral synovial whole mounts were minced in $500 \mu\text{l}$ of PBS per animal, and samples were acquired using a BD FACSVerser flow cytometer. The results were analyzed by FCAP Array v3 software (BD).

Bulk RNA-seq library construction and sequencing

The indicated cell types in each experiment were lysed using RLT Plus buffer (Qiagen), vortexed, snap-frozen on dry ice and stored at -80°C . To extract RNA from cell lysates, an RNeasy Plus Micro kit (Qiagen)

was used according to the manufacturer's instructions. Genomic DNA contamination was removed using Optimal DNA depletion columns (Qiagen). Purified RNA was eluted in nuclease-free water (Ambion) and stored at -80°C . To assess the quality and concentration of purified RNA, an RNA Pico chip (Applied Biosystems) on a Bioanalyzer 2000 (Applied Biosystems) was used according to the manufacturer's instructions. For library preparation, a SMARTer Stranded Total RNA-seq Mammalian Pico Input kit v3 (Takara) was used according to the manufacturer's instructions. Library size was assessed using a High Sensitivity DNA chip (Applied Biosystems) on a Bioanalyzer 2000 (Applied Biosystems) according to the manufacturer's instructions. Bulk RNA-seq was performed using a Novaseq 6000 (Illumina) on a $2 \times 150 \text{ bp}$ sequencing run. Pooled libraries were demultiplexed using Casava (Illumina). Fastq files from sequencing libraries were trimmed of the first three nucleotides on the R1 strand. Contaminating adaptor sequences and poor-quality bases were removed using Trim Galore (Babraham Bioinformatics). Libraries were only trimmed for quality. The quality of the resulting files was assessed by FastQC and aligned to the mm10 genome using HISAT2.

Subsequent RNA-seq analysis was performed in the R statistical environment, as described before⁵⁵, with RStudio 2022.02.2. Resulting data are available on the Gene Expression Omnibus (GEO) under accession numbers [GSE247475](https://www.ncbi.nlm.nih.gov/geo/query/acc.cgi?acc=GSE247475), [GSE247476](https://www.ncbi.nlm.nih.gov/geo/query/acc.cgi?acc=GSE247476), [GSE247477](https://www.ncbi.nlm.nih.gov/geo/query/acc.cgi?acc=GSE247477) and [GSE272541](https://www.ncbi.nlm.nih.gov/geo/query/acc.cgi?acc=GSE272541). Reads were counted and assigned to genes using the Featurecount function from the Rsubread package, and differential expression analysis was performed using DESeq2 with an appropriate design matrix according to the default workflow. Batch effects were removed using the sva package. Figures were plotted using the ggplot2 and pheatmap packages and Prism software. Gene ontology enrichment testing was performed using topGO. GSEA (<https://www.gsea-msigdb.org/gsea>) was conducted using GSEA v4.3.0 according to developer's instructions with the preranked option and classic setting. KEGG gene sets were downloaded from the Molecular Signatures Database.

Analysis of public scRNA-seq datasets

For the analysis of the dataset from [GSE145286](https://www.ncbi.nlm.nih.gov/geo/query/acc.cgi?acc=GSE145286) (ref. 6), raw data from WT mice were downloaded from the GEO archive, and count data were imported into R. After quality control, normalization and dimensional reduction, gene expression was visualized by UMAP. For Extended Data Fig. 1a–c, clusters of endothelial cells were extracted with *Pecam1* and *Cdh5* expression and reclustered. Resulting clusters were annotated using canonical marker gene expression (*Pecam1*, *Sema3g*, *Hey1*, *Podxl*, *Ackr1*, *Vwf* and *Rgcc*), and capillary endothelial cells were further extracted for Fig. 1a–c. Figures were plotted using the EnhancedVolcano and DotPlot functions. For Fig. 7a, cells were clustered using canonical marker genes (*Cd68*, *Lyve1*, *H2-Ab1*, *Cd55*, *Prg4*, *Thy1* and *Pecam1*).

Development and validation of anti-NP2

Anti-NP2 was newly raised by guinea pigs immunized with peptides Gly 107–Leu 429 (UniProtKB entry [O70340](https://www.uniprot.org/entry/O70340)).

For immunocytochemistry, HEK293 tsA201 cells (a gift from R. Horn, Thomas Jefferson University) were cultured in high-glucose DMEM (Sigma-Aldrich) containing 10% fetal bovine serum (HyClone), 50 U ml^{-1} penicillin, 50 mg ml^{-1} streptomycin (Invitrogen) and 2 mM L-glutamine at 10% CO_2 and 37°C . Cells were transfected with HA-tagged mouse NP1, NP2 or NPR in pCAGGS using Lipofectamine 2000 (Invitrogen). The following day, transfected cells were fixed with 4% paraformaldehyde (PFA) in PBS for 15 min and washed with PBS three times. After blocking/permeabilization with 3% BSA (Sigma-Aldrich) in PBS containing 0.1% Triton X-100 (Sigma-Aldrich) for 30 min, cells were stained with primary antibodies to the HA tag (mouse, 1:1,000, BAbCo, MMS-101P) and NP2CC2 (guinea pig; final concentration of $1 \mu\text{g ml}^{-1}$) for 2 h at RT, followed by washing with PBS and incubation with the respective secondary antibodies (Alexa 488 (Invitrogen) and

Cy3 (Jackson ImmunoResearch Laboratories) to the respective primary antibody; 1:1,000) for 30 min. After washing with PBS, coverslips were mounted on a glass slide with Fluoromount-G (Thermo Fisher Scientific). Fluorescence was detected using an SD-OSR microscope (Olympus).

For immunohistochemistry, mice were housed on a standard light cycle (0800–2000 h) before placement into constant darkness for 7 days. Mice were transcardially perfused with 4% PFA in 0.1 M sodium phosphate buffer (pH 7.2) for 10 min under deep pentobarbital anesthesia in the dark (0 h = control condition) or light-exposed for 4 h (4 h = light-stimulated condition) before death, followed by postfixation of dissected brain samples with 4% PFA in PBS for 2 h at 4 °C. Free-floating sagittal sections (50- μ m thickness) from brains fixed in 4% PFA were prepared with a microslicer (DTK-1000, Dosaka EM). Following washing of the sections with PBS containing 0.1% Triton X-100 (wash buffer), sections were subsequently treated with 10% donkey serum for 30 min at RT, incubated with a mixture of primary antibodies (1 μ g ml⁻¹) diluted in wash buffer overnight, washed three times, incubated with species-specific secondary antibody (Alexa 488, Invitrogen; 1:200) in wash buffer and washed again three times. Finally, sections were attached to glass slides and mounted with VECTASHIELD (Vector Laboratories). Fluorescence images of NP2 were obtained in the visual cortex using a confocal microscope (SD-OSR, Olympus) and a \times 10 objective.

Image analysis

Image analysis was performed using Imaris 9.9.1, ImageJ2 version 2.14.0/1.54f or QuPath as detailed below.

For quantification of the density of each macrophage in the indicated compartments in the synovium, whole-mount synovium images for each macrophage subset were opened in QuPath, and the positions (x and y axes) of each macrophage were quantified using the ‘Cell detection’ function. The x and y axes of the center of the synovium were subtracted from the position of each macrophage, and the distance from center was calculated. Macrophage densities were calculated by dividing the number of cells by the indicated area. Density maps were created following the step in the ‘Cell detection’ function using QuPath.

For area quantification, the Imaris analysis tool ‘percentage of material above threshold colocalization’ was used to detect the area of dextran 70 kDa, dextran 2,000 kDa, PVI over CD31, fluorescently labeled microbeads over PVI or CD31, CD32b and CGRP. For comparison of different layers of the synovium from whole-mount images, the lining layer was defined by the presence of ERTR7⁺ lining fibroblasts or lining macrophages.

For quantification of penetration depth of synovial sensory fibers, the outermost layer of the synovium (lining layer) was determined by ERTR7 staining, which identifies lining fibroblasts in the synovium. z -Stack images of synovial whole mounts were created, and the distances between each fiber (CGRP⁺ and TH⁺ fibers) and the ERTR7⁺ outermost layer were measured and averaged per mouse.

For quantification of the number of clusters of MHCII⁺ macrophages in the whole-mount synovium images, clusters were defined as MHCII⁺ macrophages attached together to form a granulomatous structure with a diameter of >30 μ m.

For analysis of the proximity of each macrophage subset to PVI⁺ capillaries, PVI⁺ capillaries and CGRP⁺ nociceptor neurons, we used the Surface module of Imaris (Bitplane)⁵⁶. Briefly, we performed multiparameter imaging of whole-mount synovium using confocal microscopy and reconstructed fluorescent staining of MHCII, CD11c, LYVE1, PVI, CD31 and CGRP separately as three-dimensional volumes using the Surface module and smooth parameters of 1.99 μ m for vessels, 1.00 μ m for cells and 0.50 μ m for neurons. Under the function ‘Set voxel intensity inside surface to 0’, we used PVI signals as a mask to determine CD31 staining outside of the PVI volume (defined as ‘CD31⁺PVI⁻ volume’) and CD11c signals as a mask to determine MHCII staining outside of

the CD11c volume (defined as ‘MHCII⁺CD11c⁻ volume’). Threshold for absolute intensity and filter for number of voxels were selected to cover signals of the region of interest, and surfaces that do not cover the region of interest were removed. We then quantified the shortest distance between the surface of each macrophage and specific capillaries or neurons, percentage of cells in direct contact with each structure and overlapped volume ratio between each macrophage and neurons. The percentage of cells in the indicated interval of distance and the mean value per animal were calculated.

Statistical analysis

The results are shown as single data points in a scatter dot plot and as mean \pm s.e.m. Between-group differences were determined using a two-tailed t -test. A one-way ANOVA with Tukey’s post hoc test was used for comparisons among three or more groups, and a one-way ANOVA with Dunnett’s test was used for comparisons of the mean of each column to the mean of a control column. Statistical analyses were performed using GraphPad Prism 8.4.1 (GraphPad Software). Animal and human sample sizes are indicated on scatter dot plots unless mentioned in the figure legend.

Reporting summary

Further information on research design is available in the Nature Portfolio Reporting Summary linked to this article.

Data availability

The datasets analyzed during the current study are available from the corresponding author upon reasonable request. Access to raw RNA-seq data related to this study is available through GEO (accession numbers [GSE247475](https://www.ncbi.nlm.nih.gov/geo/query/acc.cgi?acc=GSE247475), [GSE247476](https://www.ncbi.nlm.nih.gov/geo/query/acc.cgi?acc=GSE247476), [GSE247477](https://www.ncbi.nlm.nih.gov/geo/query/acc.cgi?acc=GSE247477) and [GSE272541](https://www.ncbi.nlm.nih.gov/geo/query/acc.cgi?acc=GSE272541)). For the reanalysis of mouse synovium scRNA-seq, we obtained the dataset from GEO (accession number [GSE145286](https://www.ncbi.nlm.nih.gov/geo/query/acc.cgi?acc=GSE145286)). The KEGG gene set is available from Molecular Signatures Database (<https://www.gsea-msigdb.org/gsea/msigdb/index.jsp>). Source data are provided with this paper.

Code availability

RNA-seq data analysis was performed in R using field-standard, previously reported packages and indicated parameters, which are described in the Methods and with the relevant source publications cited where appropriate. No custom code beyond adaptation of existing software packages was used in this study. The code is available on reasonable request from the corresponding authors.

References

- Bolland, S. & Ravetch, J. V. Spontaneous autoimmune disease in Fc γ R1B-deficient mice results from strain-specific epistasis. *Immunity* **13**, 277–285 (2000).
- Helyes, Z. et al. Transfer of complex regional pain syndrome to mice via human autoantibodies is mediated by interleukin-1-induced mechanisms. *Proc. Natl Acad. Sci. USA* **116**, 13067–13076 (2019).
- Suchanek, O. et al. Tissue-resident B cells orchestrate macrophage polarisation and function. *Nat. Commun.* **14**, 7081 (2023).
- Richoz, N. et al. Distinct pathogenic roles for resident and monocyte-derived macrophages in lupus nephritis. *JCI Insight* **7**, e159751 (2022).
- Perner, C. & Sokol, C. L. Protocol for dissection and culture of murine dorsal root ganglia neurons to study neuropeptide release. *STAR Protoc.* **2**, 100333 (2021).
- Banham, G. et al. Bromodomain inhibitors modulate Fc γ R-mediated mononuclear phagocyte activation and chemotaxis. *Front. Immunol.* **13**, 885101 (2022).
- Bissen, D., Kracht, M. K., Foss, F. & Acker-Palmer, A. Expansion microscopy of mouse brain organotypic slice cultures to study protein distribution. *STAR Protoc.* **3**, 101507 (2022).

Acknowledgements

We thank E. Johnston for technical assistance with dissecting DRGs, A. Vogt and R. Al Hosni for assistance with preparing human samples and J. Villar for assistance with collecting mouse samples. T.H. is supported by Human Frontier Science Program (LT000028/2021-L) and a Kennedy Trust senior research fellowship (KENN 23 24 15). R.S. is supported by the Wellcome Trust (215378/Z/19/Z). A.J.H. is supported by Versus Arthritis clinical research fellowship (22293). M.R.C. is supported by the National Institute of Health Research, Cambridge Biomedical Research Centre and a Wellcome Investigator Award (220268/Z/20/Z). K.S. was supported by JSPS KAKENHI (JP16H06280).

Author contributions

T.H. and M.R.C. designed the study. T.H., C.Y.C.L., N.R., A.J.H., A.F. and R.S. performed experiments. A.W.M. and M.A.B. provided human synovium specimens. K.S., M.Y. and M.W. developed and validated the antibody to NP2. N.L., K.T. and A.D. supported experiments using *Cx3cr1^{CreER}Il1b^{fl/fl}* mice. Z.L. and F.G. supported experiments using *Ms4a3^{Cre}-Rosa^{TdT}* mice. T.H. and M.R.C. wrote the manuscript.

Competing interests

The authors declare no competing interests.

Additional information

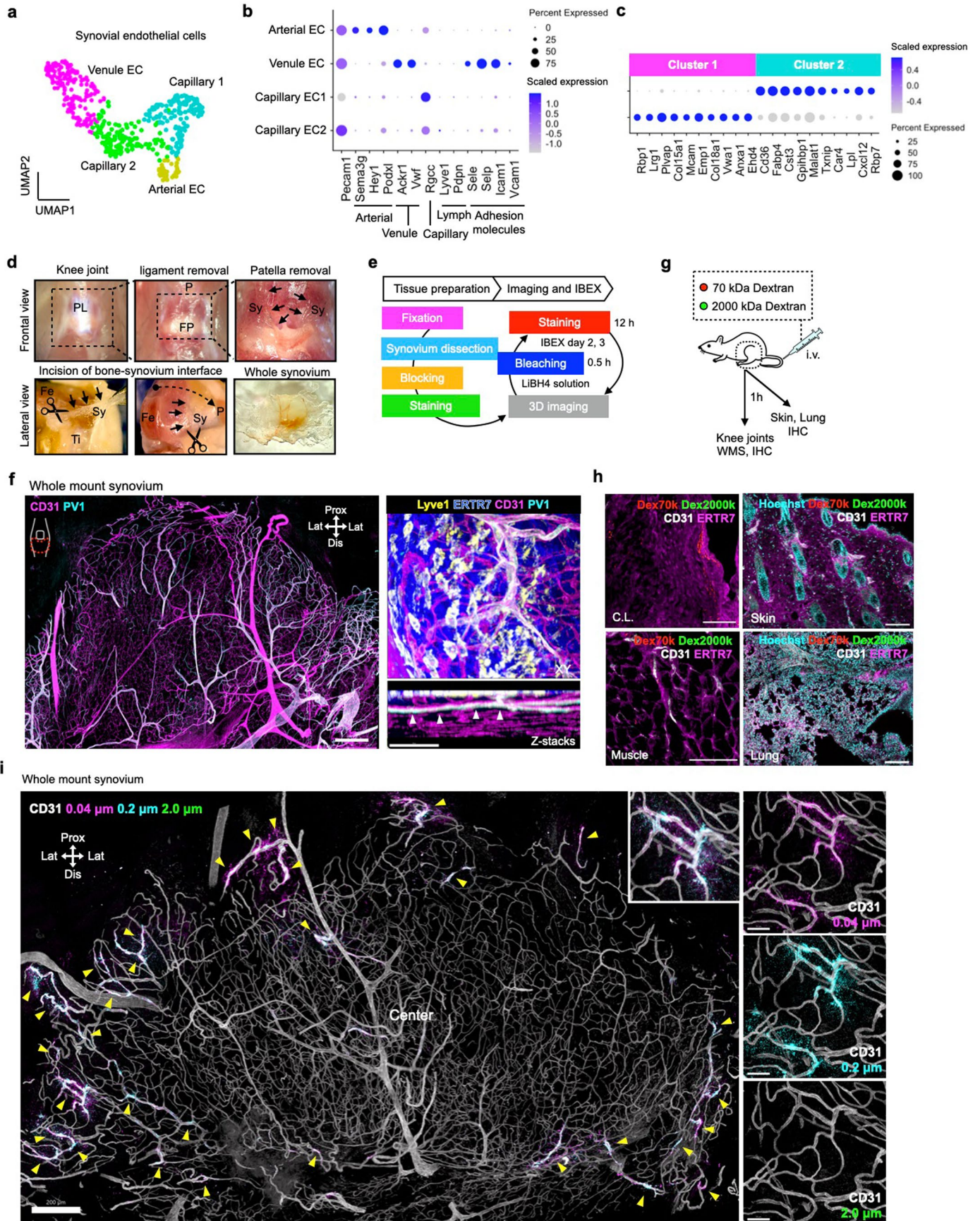
Extended data is available for this paper at <https://doi.org/10.1038/s41590-024-02011-8>.

Supplementary information The online version contains supplementary material available at <https://doi.org/10.1038/s41590-024-02011-8>.

Correspondence and requests for materials should be addressed to Tetsuo Hasegawa or Menna R. Clatworthy.

Peer review information *Nature Immunology* thanks Clifford Woolf and the other, anonymous, reviewer(s) for their contribution to the peer review of this work. Primary Handling Editor: S. Houston, in collaboration with the *Nature Immunology* team.

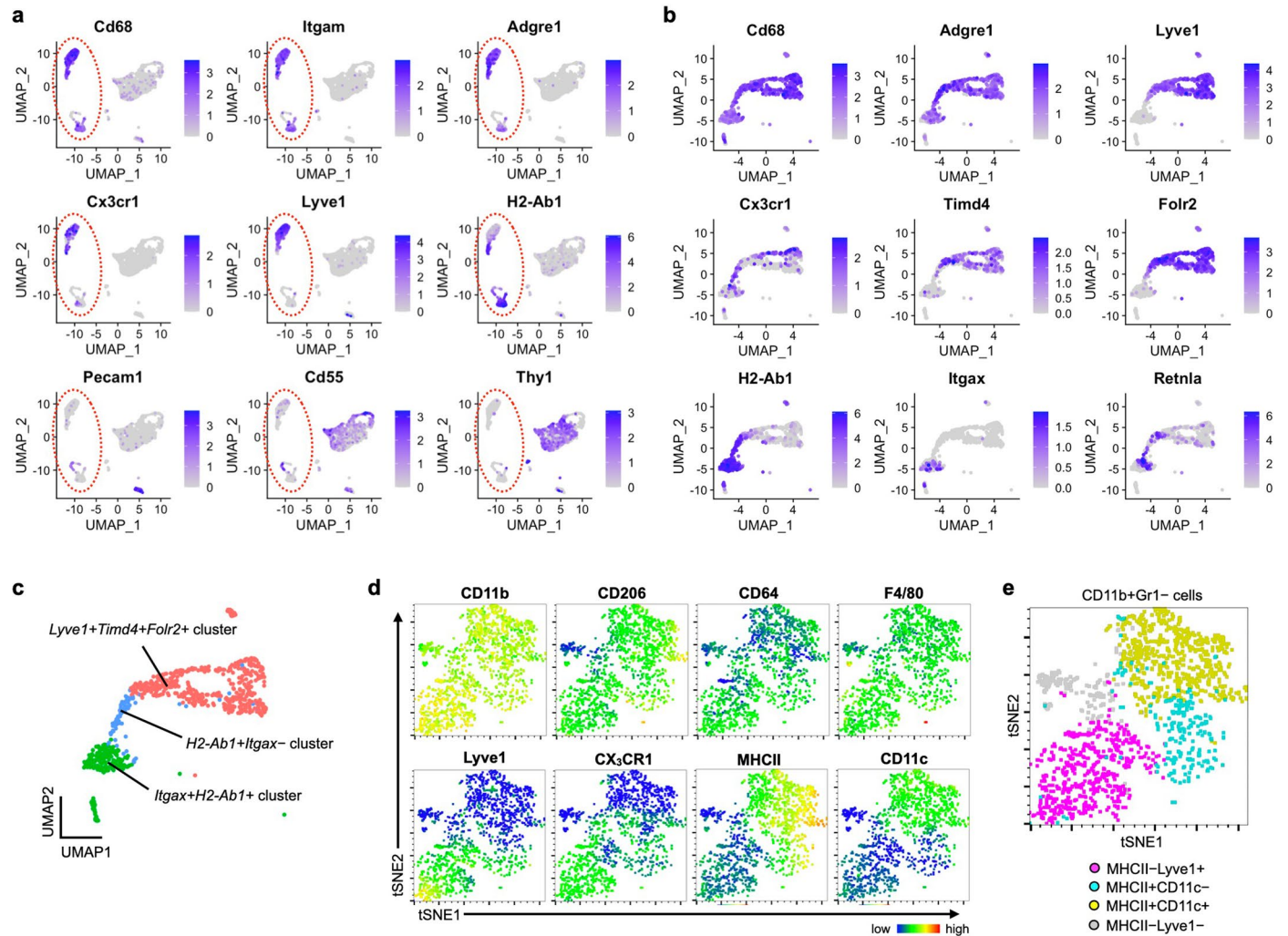
Reprints and permissions information is available at www.nature.com/reprints.



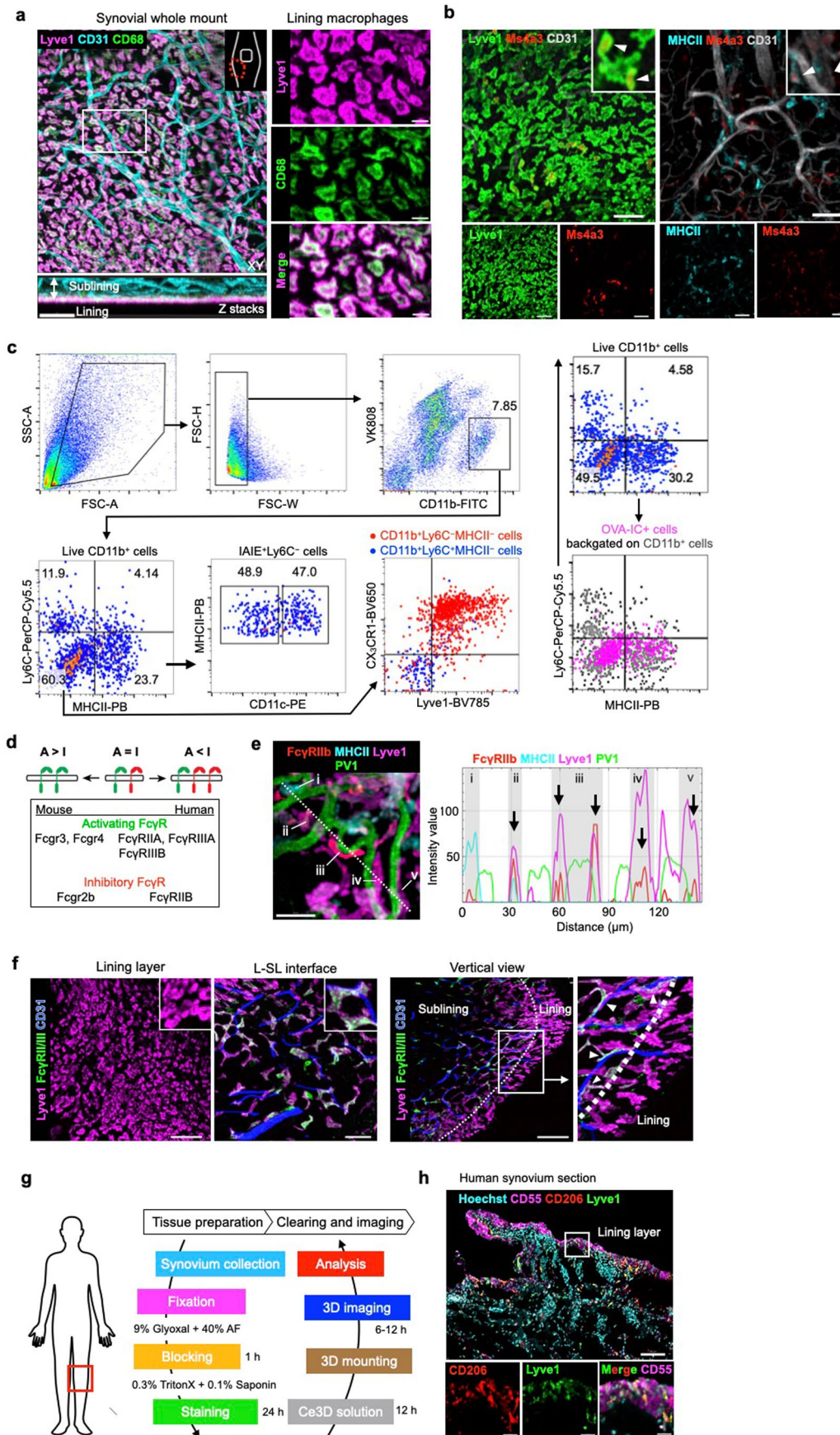
Extended Data Fig. 1 | See next page for caption.

Extended Data Fig. 1 | PVI+ capillaries with distinct molecular signatures localised at the L-SL interface of the synovium. (a) Uniform manifold approximation and projection (UMAP) visualizations of Pecam1+ endothelial cells in synovium. ScRNA-seq data from [GSE145286](#). (b) Dot plots showing the scaled gene expression and percentage of cells expressing genes for cell markers and adhesion molecules in endothelial cell populations from scRNA-seq analysis. (c) Top 10 differentially expressed genes between two cell populations in synovial capillary endothelial cells. (d) Anatomic localization of the synovium from the frontal view and dissection protocol from the lateral view. P: patella, PL: patella ligament, FP: fat pad, Sy: synovium, Fe: femur, Ti: tibia. (e) Schematic depicting tissue preparation, imaging and iterative bleaching extends multiplexity (IBEX) protocol. (f) 3D reconstruction of representative confocal images of whole

mount synovium. Arrowheads indicate PVI+ capillaries at the lining-sublining (L-SL) interface (Z-stack images). Bars, 200 and 50 μm . Images are representative of at least three independent experiments with similar results. (g) Schematic diagram showing the protocol. (h) Representative confocal images of sections of skin and lung from wild type mice injected i.v. with 70 and 2000 kDa Dextran (300 μg 70 kDa Dextran and 150 μg 2000 kDa Dextran) 1 h prior to analysis. Images are representative of at least three independent experiments with similar results. (i) 3D reconstruction of representative confocal images of whole mount synovium from wild type mice injected i.v. with fluorescently labeled microbeads of different sizes 1 h prior to analysis. Arrows indicate the sites where microbeads extravasated. Bars, 200 and 50 μm . Images are representative of at least three independent experiments with similar results.



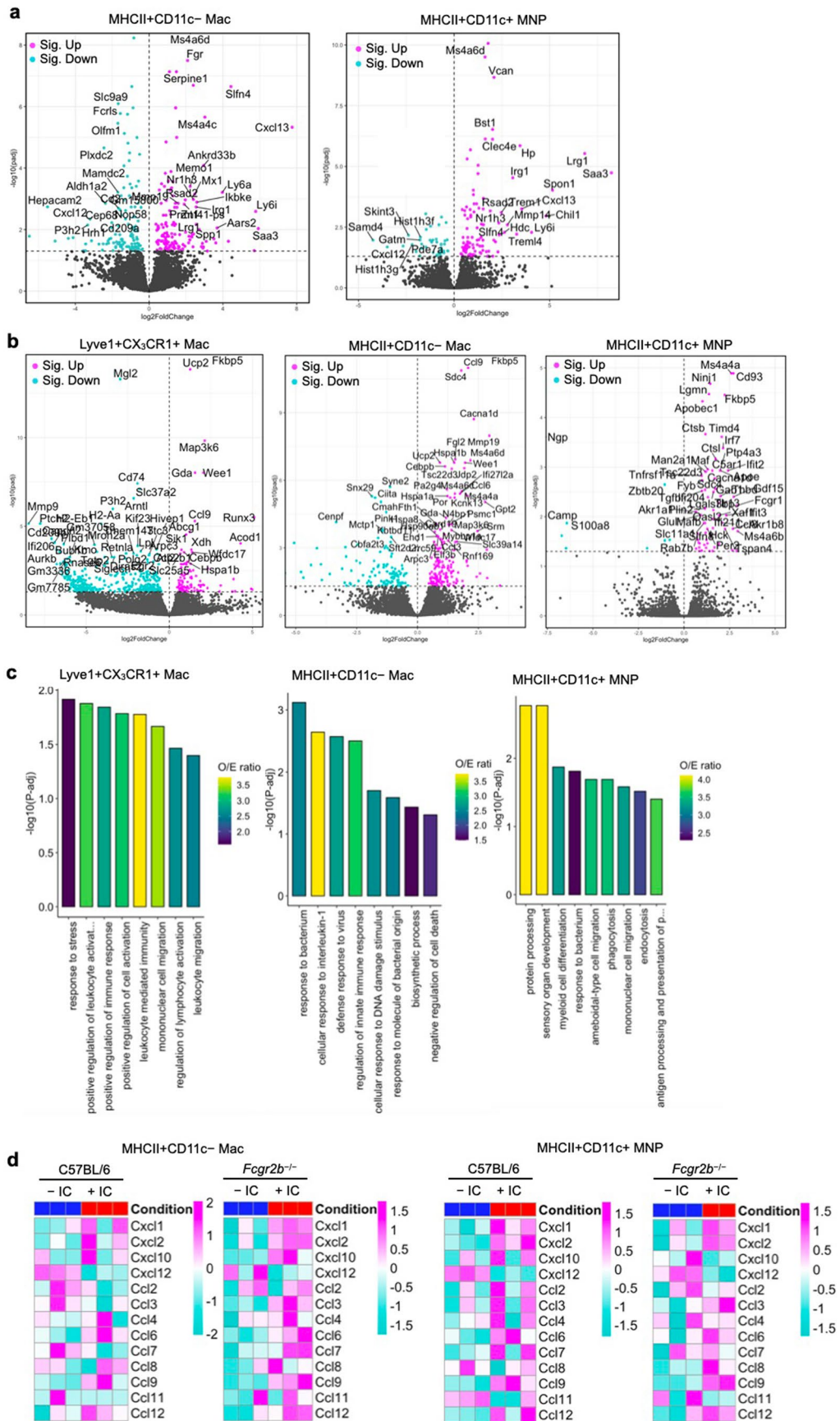
Extended Data Fig. 2 | Gating strategy for healthy synovial macrophages. (a) UMAP visualisations of the healthy synovium and (b, c) myeloid cells (red circle) in the same dataset. ScRNA-seq data from [GSE145286](https://www.ncbi.nlm.nih.gov/geo/query/acc.cgi?acc=GSE145286). (d, e) tSNE plot of surface marker expressions of CD11b + Gr1⁻ cells in the healthy synovium using flow cytometry. Data from 6 mice were concatenated.



Extended Data Fig. 3 | See next page for caption.

Extended Data Fig. 3 | IC uptake and localisation of macrophages expressing FcγRII/III in the synovium. (a) 3D reconstruction of representative confocal images of whole mount synovium. Bars, 50 (left) and 10 μm (right). Images are representative of at least three independent experiments with similar results. (b) 3D reconstruction of representative confocal images of whole mount synovium from Ms4a3^{Cre}-Rosa^{tdT} mice. Bars, 50 μm. (c) Gating strategy and flow cytometric analysis of OVA-IC uptake by synovial macrophages from wild type mice injected i.v. with OVA-AF647;RaOVA (40 μg OVA-AF647 + 150 μg RaOVA) 2 h prior to analysis. Plots are representative of 3 mice. (d) Schematic of FcγR A:I ratios. (e) Representative plot profile intensity of cells (right) as indicated by

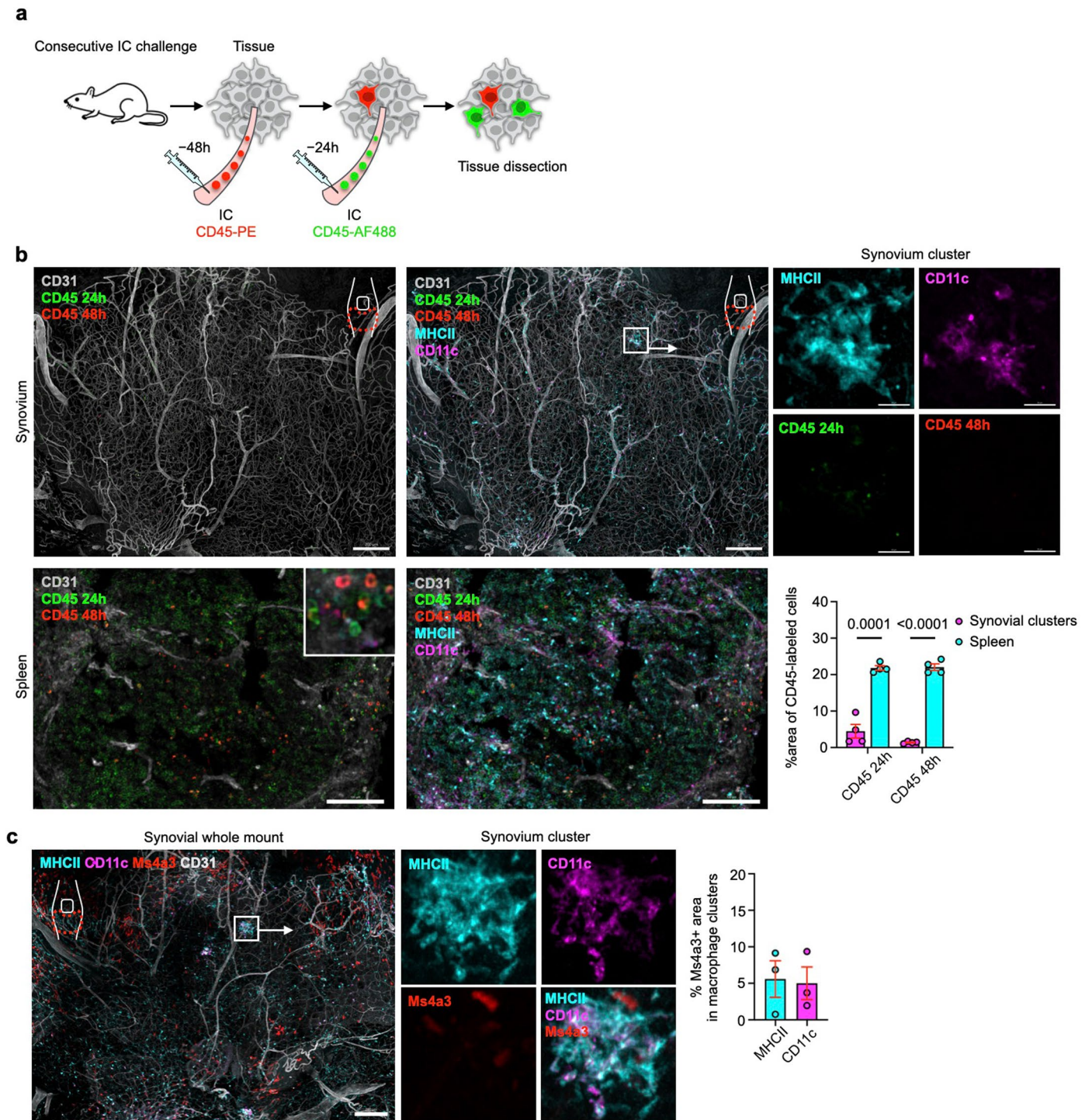
the white line shown in the 3D reconstruction of representative confocal images of L-SL interface of whole mount synovium (left), showing five representative cells consisting of MHCII+ cells and Lyve1+ cells. Images are representative of at least two independent experiments with similar results. (f) 3D reconstruction of representative confocal images of indicated layer of whole mount synovium. Bars, 50 μm. Arrowheads indicate FcγRII/III+ area at L-SL interface. (g) Schematic depicting tissue preparation, clearing, and imaging protocol of human synovium. (h) Representative confocal images of sections of human synovium. CD55+ area represents lining fibroblasts. Bars, 100 and 20 μm. Images are representative of at least two independent experiments with similar results.



Extended Data Fig. 4 | See next page for caption.

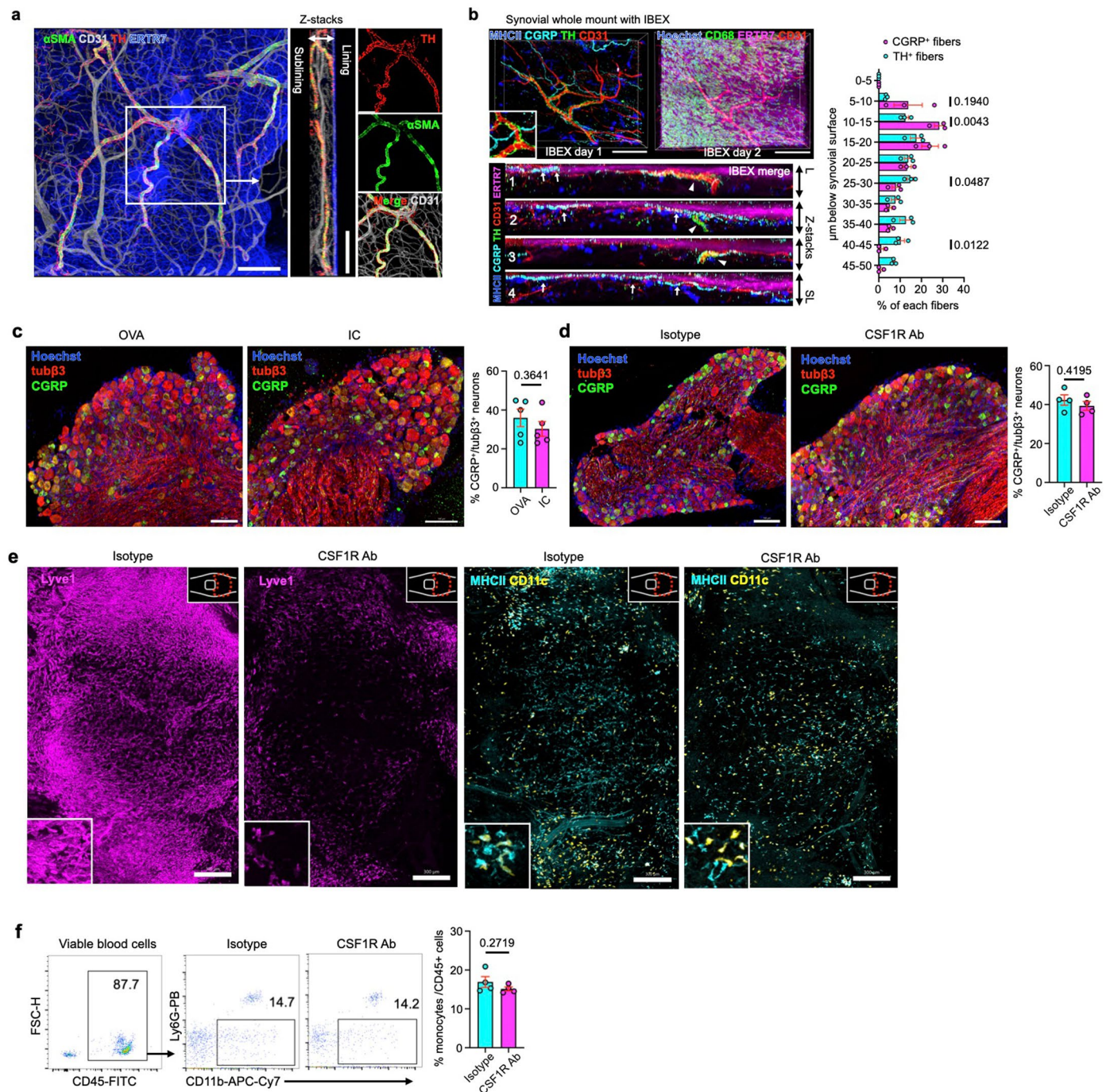
Extended Data Fig. 4 | Depletion of FcγRIIb alters the response to IC in each synovial macrophage subset. (a) Volcano plots showing DEGs due to OVA-IC stimulation in MHCII+CD11c⁻ and MHCII+CD11c⁺ macrophages from wild type mice by RNA-seq. Wald test was used. (b) Volcano plots showing DEGs due to OVA-IC stimulation in Lyve1⁺, MHCII+CD11c⁻, and MHCII+CD11c⁺

macrophages from Fcgr2b^{-/-} mice by RNA-seq. Wald test was used. (c) Gene ontology (GO) analysis of DEGs specific to each macrophage subset with all the DEGs of 3 subsets as the background gene list. (d) Heat map of expression of chemokines with or without IV IC injection in MHCII+CD11c⁻ and MHCII+CD11c⁺ macrophages from wild type and Fcgr2b^{-/-} mice (scaled normalized values).



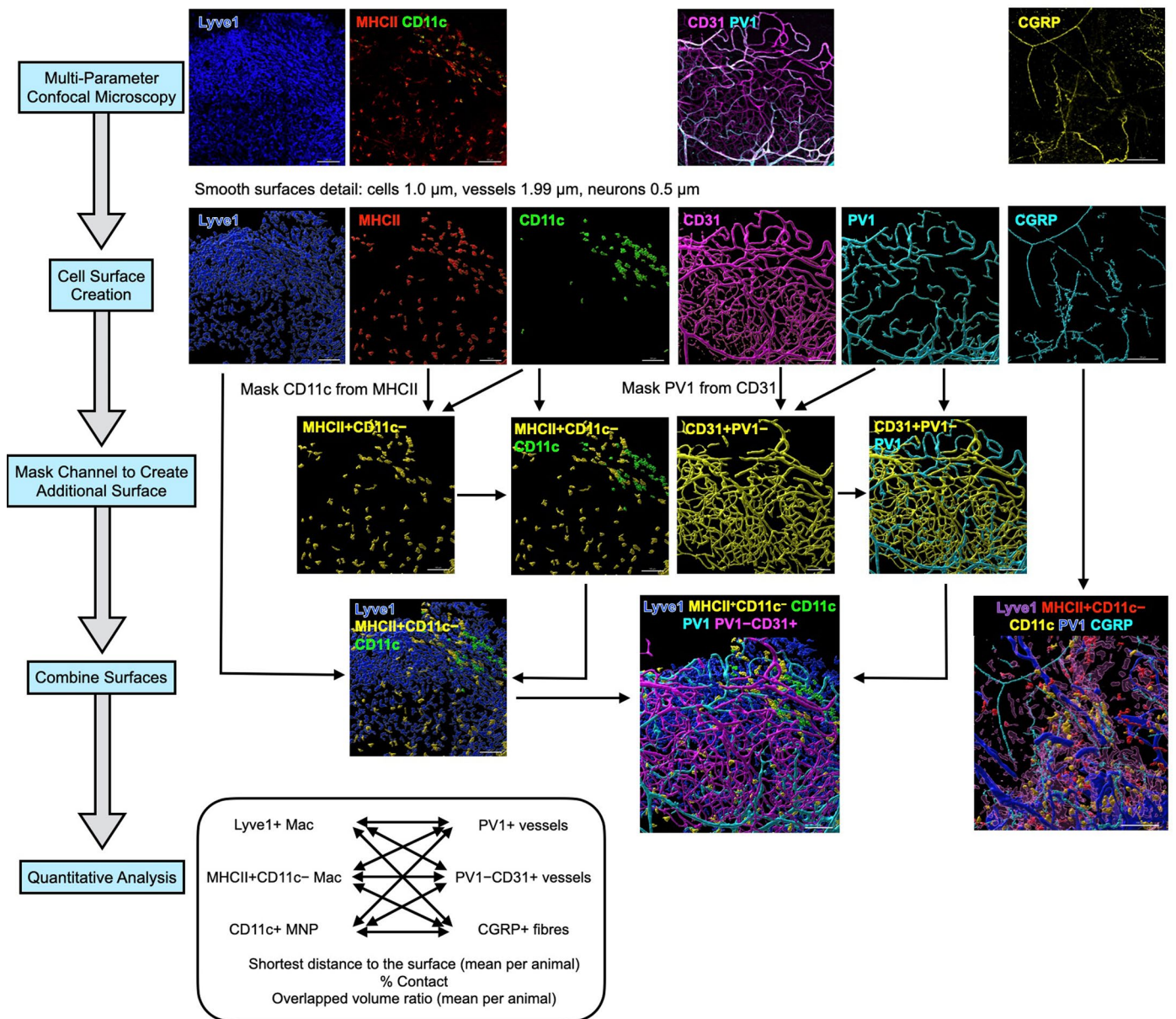
Extended Data Fig. 5 | Monocyte contribution in the formation of MHCII+ macrophage clusters. (a) Schematic depicting the experiment. (b) 3D reconstruction of representative confocal images of whole mount synovium and sectional images of spleen after IC and anti-CD45 antibody injection.

Bars, 200 (synovium) and 100 μ m (spleen). Data represents mean \pm SEM. Two-tailed t test was used. (c) 3D reconstruction of representative confocal images of whole mount synovium from *Ms4a3^{Cre}-Rosa^{TDT}* mice. Bars, 200 μ m. Data represents mean \pm SEM.

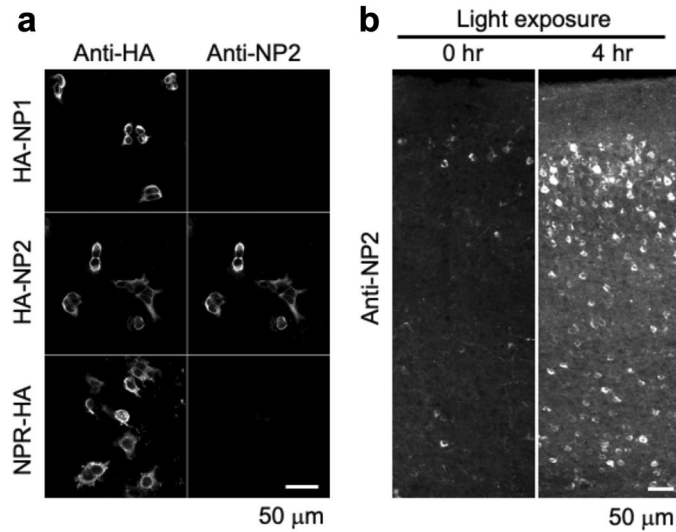


Extended Data Fig. 7 | Distribution of TH⁺ and CGRP⁺ fibres in the synovium using IBEX. (a) 3D reconstruction of representative confocal images of whole mount synovium stained for tyrosine hydroxylase (TH). Bars, 100 μm. Images are representative of at least three independent experiments with similar results. **(b)** 3D reconstruction of representative confocal images of iterative bleaching extends multiplexity (IBEX) of whole mount synovium. Bars, 100 μm. Four Z-stack images of IBEX of whole mount synovium (bottom). Quantification of the penetration depth of CGRP⁺ and TH⁺ fibres as a percentage among total fibres for each subset (right). n = 3 mice for each group. **(c)** Representative confocal

images of L4 dorsal root ganglia (DRG) from mice intravenously injected with OVA or IC. Bars, 100 μm. n = 5 mice for each group. **(d)** Representative confocal images of L4 DRG from mice intraperitoneally injected with isotype control or anti-CSF1R antibody. Bars, 100 μm. n = 4 mice for each group. **(e)** Enlarged images for each macrophage subset in Fig. 6e. **(f)** Flow cytometry plot showing the number of monocytes from mice intraperitoneally injected with isotype control or anti-CSF1R antibody 72 h prior to assessment. Data represents mean ± SEM and two-tailed t test was used for in **b, c, d, f**.

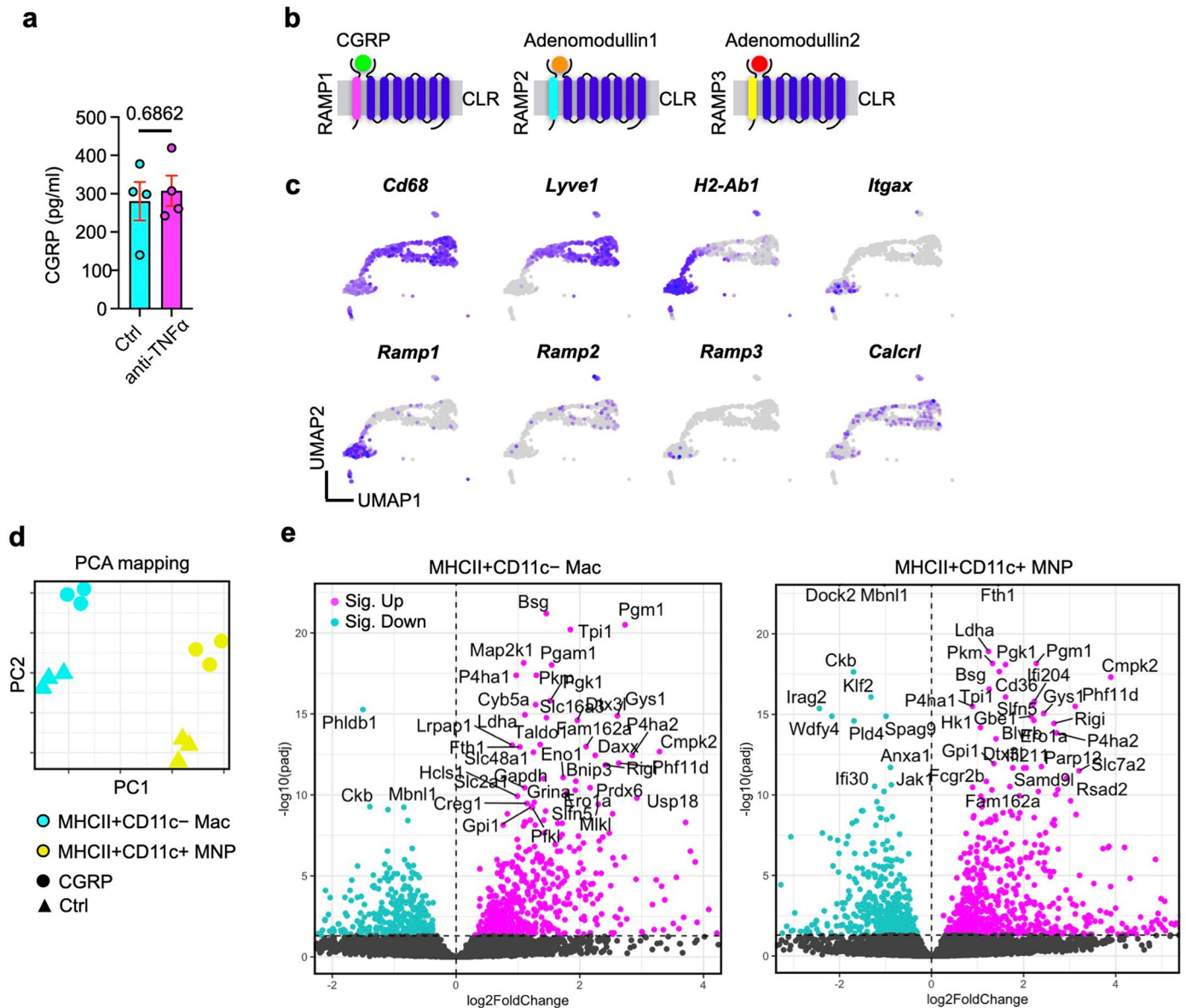


Extended Data Fig. 8 | Protocol for quantifying spatial distribution of three types of macrophages, vessels, and CGRP⁺ fibres. Multi-parameter imaging of whole mount synovium was reconstructed with each fluorescent staining and quantitative analysis was performed.



Extended Data Fig. 9 | Validation of anti-NP2 antibody. (a) Immunocytochemical analysis of HA-tagged NP1, NP2 and NPR (full-length) expressed in HEK293 cells. Newly raised anti-NP2 antibody showed selective signals for NP2. (b) Specific immunostaining of endogenous NP2 in the visual cortex after

the light stimulation. Anti-NP2 antibody detected the increase of NP2 protein expression in all layers of visual cortex 4 hours after light exposure compared with 0 hr exposure control. Bars, 50 μm.



Extended Data Fig. 10 | CGRP induces distinct transcriptional changes in MHCII+CD11c⁻ and MHCII+CD11c⁺ macrophages. (a) CGRP ELISA of DRG culture supernatants stimulated with supernatants from IC stimulated synovial explant. TNF neutralizing antibodies (4 $\mu\text{g}/\text{ml}$) or isotype control were added to synovial supernatants before adding to DRG neurons. $n = 4$ mice for each group. Data represents mean \pm SEM. Two-tailed t test was used. (b) Illustration of receptor activity-modifying protein (RAMP) association on calcitonin receptor-like receptor (CLR). (c) Expression of marker genes for macrophages and

neuropeptide receptors in healthy synovium. scRNA-seq data from GSE145286. (d) Principle component analysis (PCA) of MHCII+CD11c⁻ and MHCII+CD11c⁺ macrophages from synovial explant of WT mice treated with 100 nM CGRP or control for 4 hours by RNA-seq. $n = 3$ mice were compiled for each plot and $n = 18$ mice for each population. (e) Volcano plots showing differentially expressed genes in MHCII+CD11c⁻ and MHCII+CD11c⁺ macrophages with CGRP stimulation. Wald test was used.

Reporting Summary

Nature Portfolio wishes to improve the reproducibility of the work that we publish. This form provides structure for consistency and transparency in reporting. For further information on Nature Portfolio policies, see our [Editorial Policies](#) and the [Editorial Policy Checklist](#).

Statistics

For all statistical analyses, confirm that the following items are present in the figure legend, table legend, main text, or Methods section.

n/a Confirmed

- The exact sample size (n) for each experimental group/condition, given as a discrete number and unit of measurement
- A statement on whether measurements were taken from distinct samples or whether the same sample was measured repeatedly
- The statistical test(s) used AND whether they are one- or two-sided
Only common tests should be described solely by name; describe more complex techniques in the Methods section.
- A description of all covariates tested
- A description of any assumptions or corrections, such as tests of normality and adjustment for multiple comparisons
- A full description of the statistical parameters including central tendency (e.g. means) or other basic estimates (e.g. regression coefficient) AND variation (e.g. standard deviation) or associated estimates of uncertainty (e.g. confidence intervals)
- For null hypothesis testing, the test statistic (e.g. F , t , r) with confidence intervals, effect sizes, degrees of freedom and P value noted
Give P values as exact values whenever suitable.
- For Bayesian analysis, information on the choice of priors and Markov chain Monte Carlo settings
- For hierarchical and complex designs, identification of the appropriate level for tests and full reporting of outcomes
- Estimates of effect sizes (e.g. Cohen's d , Pearson's r), indicating how they were calculated

Our web collection on [statistics for biologists](#) contains articles on many of the points above.

Software and code

Policy information about [availability of computer code](#)

Data collection

CytoFLEX LX (Beckman Coulter) for FACS, FACSAria Fusion (Becton Dickinson) for cell sorting, TCS SP8 inverted confocal microscope (Leica Microsystems) for confocal imaging, TCS SP8 3X gated STED confocal inverted microscope (Leica Microsystems) for confocal imaging, Zeiss 710 NLO upright multiphoton microscope (Zeiss) for multiphoton imaging, stereoscopic microscope (Stemi 2000-CS, Zeiss) for synovium dissection, Illumina NovaSeq 6000 for RNA sequencing. BD FACSVerser flow cytometer (Becton Dickinson) for cytometric bead array.

Data analysis

Imaris version 9.9.1, FlowJo version 10.6.2, ImageJ2 version 2.14.0/1.54f, QuPath version 0.3.2, Prism version 8.4.1, FCAP Array v3 software. RNA-seq analysis was performed in the R statistical environment with RStudio 2022.02.2. Resulting data is available on GEO under accession numbers GSE247475, GSE247476, GSE247477, and GSE272541. Reads were counted and assigned to genes using the Featurecount function from the Rsubread package and differential expression analysis was performed using DESeq2 with an appropriate design matrix according to the default workflow, and batch effects removed using the sva package. Figures were plotted using the ggplot2, pheatmap packages and Prism software. Gene ontology enrichment testing was performed using topGO. Gene Set Enrichment Analysis (GSEA, <https://www.gsea-msigdb.org/gsea>) was conducted using GSEA v4.3.0 according to developers' instruction, using the pre-ranked option and classic setting. Kegg gene set was downloaded from Molecular Signature Database (MSigDB). No custom code beyond adaptation of existing software packages were used in this study. The code is available on reasonable request from the corresponding author.

For manuscripts utilizing custom algorithms or software that are central to the research but not yet described in published literature, software must be made available to editors and reviewers. We strongly encourage code deposition in a community repository (e.g. GitHub). See the Nature Portfolio [guidelines for submitting code & software](#) for further information.

Data

Policy information about [availability of data](#)

All manuscripts must include a [data availability statement](#). This statement should provide the following information, where applicable:

- Accession codes, unique identifiers, or web links for publicly available datasets
- A description of any restrictions on data availability
- For clinical datasets or third party data, please ensure that the statement adheres to our [policy](#)

Access to raw RNA-seq data related to this study is available through the Gene Expression Omnibus (GEO) (accession number: GSE247475, GSE247476, GSE247477, and GSE272541). For the reanalysis of mouse synovium single-cell RNA sequencing, we obtained the dataset from GEO (the accession number: GSE145286). Kegg gene set is available from Molecular Signature Database (<https://www.gsea-msigdb.org/gsea/msigdb/index.jsp>). Source Data are provided with this paper.

Research involving human participants, their data, or biological material

Policy information about studies with [human participants or human data](#). See also policy information about [sex, gender \(identity/presentation\), and sexual orientation](#) and [race, ethnicity and racism](#).

Reporting on sex and gender	In human study, samples were collected without regard to gender.
Reporting on race, ethnicity, or other socially relevant groupings	Because of the recruitment protocol stated below, samples from UK citizens were only used in this study.
Population characteristics	Human synovial specimens were obtained from osteoarthritis patients undergoing replacement surgery or synovectomy with prior ethical approval (REC: 18/NW/0545) and informed consent at Addenbrooke's Hospital, Cambridge. Samples were obtained from 2 male and 3 female donors aged 57-83.
Recruitment	Human synovial specimens were obtained from osteoarthritis patients undergoing replacement surgery or synovectomy. The presence of osteoarthritis and their age distribution may have potential bias to the results, which can show more inflammatory phenotype than healthy subjects.
Ethics oversight	Researches using human subjects in this study are approved with prior ethical approval (REC: 18/NW/0545) at Addenbrooke's Hospital, Cambridge.

Note that full information on the approval of the study protocol must also be provided in the manuscript.

Field-specific reporting

Please select the one below that is the best fit for your research. If you are not sure, read the appropriate sections before making your selection.

- Life sciences Behavioural & social sciences Ecological, evolutionary & environmental sciences

For a reference copy of the document with all sections, see [nature.com/documents/nr-reporting-summary-flat.pdf](https://www.nature.com/documents/nr-reporting-summary-flat.pdf)

Life sciences study design

All studies must disclose on these points even when the disclosure is negative.

Sample size	We did not use statistical methods to predetermine sample sizes. We estimated the required sample sizes by considering variations and means of preliminary results, and sought to reach reliable conclusions with as small sample size as possible. Previously published results, experimental complexity, the cost of experiments and past experiences were used to determine the sample sizes although we did not refer to any specific previous study.
Data exclusions	No data were excluded.
Replication	Experiments included sufficient sample size to ensure the reproducibility of the findings. Representative data was confirmed at least twice by performing independent experiments. All attempts at replication were successful.
Randomization	The animals were randomly assigned to each treatment/control group within each genotype. For human experiments, parameters were compared within the specimen from same patients. Therefore, randomisation wasn't applied.
Blinding	Investigators were aware of the group allocation because the treatment groups needed to be clear when performing the experiments.

Reporting for specific materials, systems and methods

Materials & experimental systems

n/a	Included in the study
<input type="checkbox"/>	<input checked="" type="checkbox"/> Antibodies
<input type="checkbox"/>	<input checked="" type="checkbox"/> Eukaryotic cell lines
<input checked="" type="checkbox"/>	<input type="checkbox"/> Palaeontology and archaeology
<input type="checkbox"/>	<input checked="" type="checkbox"/> Animals and other organisms
<input checked="" type="checkbox"/>	<input type="checkbox"/> Clinical data
<input checked="" type="checkbox"/>	<input type="checkbox"/> Dual use research of concern
<input checked="" type="checkbox"/>	<input type="checkbox"/> Plants

Methods

n/a	Included in the study
<input checked="" type="checkbox"/>	<input type="checkbox"/> ChIP-seq
<input type="checkbox"/>	<input checked="" type="checkbox"/> Flow cytometry
<input checked="" type="checkbox"/>	<input type="checkbox"/> MRI-based neuroimaging

Antibodies

Antibodies used

Information of all the antibodies used in this study is provided in detail (catalog number, clone type, lot number, supplier name) in Supplementary Table 1.

Rat anti-CD16/32 Biologend Cat# 156604, Lot# B293349, Clone S17011E
 Pacific Blue-conjugated rat anti-I-A/I-E Biologend Cat# 107620, Lot#B252427, Clone M5/114.15.2
 eFluor450-conjugated rat anti-CD3e Invitrogen Cat#48-0031-82, Lot#2102873, Clone 145-2C11
 FITC-conjugated rat anti-CD11b Biologend Cat# 101206, Lot#B286843, Clone M1/70
 AF488-conjugated rat anti-panendothelial cell antigen Biologend Cat# 120506, Lot#B277044, Clone MECA-32
 AF488-conjugated mouse anti-tubulin β 3 Biologend Cat#801203, Lot#B332149, Clone TUJ1
 AF488-conjugated rat anti-CD68 Biologend Cat# 137012, Lot# B272230, Clone FA-11
 AF488-conjugated rat anti-CD31 Biologend Cat# 102514, Lot# B282351, Clone MEC13.3
 AF488-conjugated rat anti-I-A/I-E Biologend Cat# 107616, Lot# B343353, Clone M5/114.15.2
 PerCP-Cyanine5.5-conjugated rat anti-Ly6C Invitrogen Cat# 45-5932-82, Lot#2162018, Clone HK1.4
 PerCP-Cyanine5.5-conjugated rat anti-CD206 Biologend Cat# 141716, Lot# B270129, Clone C068C2
 PE-conjugated rat anti-Tim-4 Biologend Cat# 130005, Lot# B283682, Clone RMT4-54
 PE-conjugated Armenian hamster anti-CD11c Biologend Cat# 117308, Lot# B202498, Clone N418
 PE-conjugated Syrian hamster anti-podoplanin Biologend Cat# 127407, Lot# B328276, Clone 8.1.1
 PE-conjugated mouse anti-CD32b Invitrogen Cat# 12-0321-82, Lot# 2157123, Clone AT130-2
 PE-conjugated Armenian hamster anti-CD16.2 Biologend Cat# 149503, Lot# B273077, Clone 9E9
 PE-conjugated rat anti-Lyve1 R&D systems Cat# FAB2125P, Lot# ACFE0220031, Polyclonal
 PE-Cyanine7-conjugated rat anti-Lyve1 Invitrogen Cat# 25-0443-80, Lot# 2343412, Clone ALY7
 PE-Cyanine7-conjugated rat anti-F4/80 Invitrogen Cat# 25-4801-82, Lot# 2279168, Clone BM8
 PE-Cyanine7-conjugated rat anti-CD206 (MMR) Invitrogen Cat# 25-2061-82, Lot# 2062662, Clone MR6F3
 eFluor660-conjugated rat anti-Lyve1 Invitrogen Cat# 50-0443-82, Lot# 2205461, Clone ALY7
 APC-conjugated rat anti-Ly6C Invitrogen Cat# 17-5932-82, Lot# 2002701, Clone HK1.4
 APC-conjugated rat anti-CD16 Biologend Cat# 158005, Lot# B311445, Clone S17014E
 APC-conjugated mouse anti-CD64 Biologend Cat# 139306, Lot# B277148, Clone X54-5/7.1
 APC-conjugated mouse anti-CD32b Invitrogen Cat# 17-0321-80, Lot# 2036645, Clone AT130-2
 APC-eFluor780-conjugated rat anti-Gr-1 Invitrogen Cat# 47-5931-82, Lot# 2320762, Clone RB6-8C5
 AF594-conjugated rat anti-CD31 Biologend Cat# 102520, Lot# B368931, Clone MEC13.3
 AF647-conjugated rat anti-CD31 Biologend Cat# 102516, Lot# B308659, Clone MEC13.3
 AF647-conjugated Armenian hamster anti-CD11c Biologend Cat# 117312, Lot# B341497, Clone N418
 AF647-conjugated rat anti-B220 BD Pharmingen Cat# 557683, Lot# 9123764, Clone RA3-6B2
 AF647-conjugated rat anti-ER-TR7 Novus Biologicals Cat# NB100-64932AF647, Lot# D102142, Clone ER-TR7
 APC-Cy7-conjugated rat anti-Ly6G BD Pharmingen Cat# 560600, Lot# 8277987, Clone 1A8
 Brilliant Violet421-conjugated rat anti-F4/80 Biologend Cat# 123131, Lot# B258771, Clone BM8
 Brilliant Violet605-conjugated rat anti-I-A/I-E Biologend Cat# 107639, Lot# B293222, Clone M5/114.15.2
 Brilliant Violet650-conjugated mouse anti-CX3CR1 Biologend Cat# 149033, Lot# B301229, Clone SA011F11
 Goat anti-CGRP Abcam Cat# ab36001, Lot# GR3445403-5, Polyclonal
 Rabbit anti-tyrosine hydroxylase Abcam Cat# ab112, Lot# GR3435522-1, Polyclonal
 Rabbit anti-tub β 3 Abcam Cat# ab18207, Lot# GR3257458-1, polyclonal
 Biotin-conjugated mouse anti- Ea52-68 peptide bound to I-Ab Invitrogen Cat# 13-5741-82, Lot# 1947272, Clone YAE
 Guinea pig anti-NP2 In house NA
 AF488-conjugated mouse anti-alpha smooth muscle actin Abcam Cat# AB184675, Lot# 1040301-1, Clone 1A4
 AF594-conjugated donkey anti-guinea Pig Jackson ImmunoResearch Cat# 706-585-148, Polyclonal
 AF594-conjugated mouse anti-CD31 Biologend Cat# 303126, Lot# B297139, Clone WN59
 AF647-conjugated mouse anti-CD55 Novus Biologicals Cat# NBP2-47964AF647, Lot# D105865, Clone 143-30
 AF647-conjugated mouse anti-HLA-DR Abcam Cat# ab223907, Lot# GR3441855-1, Clone TAL1B5
 Goat anti-CD32B Abcam Cat# AB77093, Lot# 1034248-3, Polyclonal
 Goat anti-LYVE1 R&D systems Cat# AF2089, Lot# KPY0119121, Polyclonal
 Rabbit anti-PLVAP Novus Biologicals Cat# NBP1-83911, Lot# 000007304, Polyclonal
 Rabbit anti-LYVE1 Abcam Cat# ab33682, Lot# GR295168-4, polyclonal
 PE/Dazzle594-conjugated mouse anti-CD206 Biologend Cat# 321130, Lot# B271255, Clone 15-2
 Anti-mouse CSF1R (CD115) Biocell Cat# BE0213, Lot# 808022M2, Clone AFS98
 Anti-mouse TNF α Biocell Cat# BE0058, Lot# 728222J1, Clone XT3.11
 Anti-mouse CXCL1 R&D systems Cat# MAB453, Lot#AOS0823041, Clone 48415

Validation

Antibodies used in this study are commercially available and have been validated by the manufacturers. Validation statements are provided on the manufacture's website.

Rat anti-CD16/32 Biologend Cat# 156604
<https://www.biologend.com/en-gb/products/trustain-fcx-plus-anti-mouse-cd16-32-antibody-17085>

Pacific Blue-conjugated rat anti-I-A/I-E Biologend Cat# 107620
<https://www.biologend.com/en-gb/products/pacific-blue-anti-mouse-i-a-i-e-antibody-3136?GroupID=BLG11931>

eFluor450-conjugated rat anti-CD3e Invitrogen Cat#48-0031-82
<https://www.thermofisher.com/antibody/product/CD3e-Antibody-clone-145-2C11-Monoclonal/48-0031-82>

FITC-conjugated rat anti-CD11b Biologend Cat# 101206
<https://www.biologend.com/en-gb/search-results/fitc-anti-mouse-human-cd11b-antibody-347?GroupID=BLG10660>

AF488-conjugated rat anti-panendothelial cell antigen Biologend Cat# 120506
<https://www.biologend.com/en-gb/products/alexa-fluor-488-anti-mouse-panendothelial-cell-antigen-antibody-3074>

AF488-conjugated mouse anti-tubulin β 3 Biologend Cat#801203
<https://www.biologend.com/nl-be/products/alexa-fluor-488-anti-tubulin-beta-3-tubb3-antibody-10828?GroupID=GROUP686>

AF488-conjugated rat anti-CD68 Biologend Cat# 137012
<https://www.biologend.com/nl-be/products/alexa-fluor-488-anti-mouse-cd68-antibody-6619>

AF488-conjugated rat anti-CD31 Biologend Cat# 102514
<https://www.biologend.com/nl-be/products/alexa-fluor-488-anti-mouse-cd31-antibody-3093>

AF488-conjugated rat anti-I-A/I-E Biologend Cat# 107616
<https://www.biologend.com/nl-be/products/alexa-fluor-488-anti-mouse-i-a-i-e-antibody-3134>

PerCP-Cyanine5.5-conjugated rat anti-Ly6C Biologend Cat# 45-5932-82
<https://www.thermofisher.com/antibody/product/Ly-6C-Antibody-clone-HK1-4-Monoclonal/45-5932-82>

PerCP-Cyanine5.5-conjugated rat anti-CD206 Biologend Cat# 141716
<https://www.biologend.com/en-gb/products/percp-cyanine5-5-anti-mouse-cd206-mmr-antibody-8477?GroupID=BLG9506>

PE-conjugated rat anti-Tim-4 Biologend Cat# 130005
<https://www.biologend.com/en-gb/products/pe-anti-mouse-tim-4-antibody-5242>

PE-conjugated Armenian hamster anti-CD11c Biologend Cat# 117308
<https://www.biologend.com/en-gb/products/pe-anti-mouse-cd11c-antibody-1816>

PE-conjugated Syrian hamster anti-podoplanin Biologend Cat# 127407
<https://www.biologend.com/en-gb/products/pe-anti-mouse-podoplanin-antibody-4882>

PE-conjugated mouse anti-CD32b Invitrogen Cat# 12-0321-82
<https://www.thermofisher.com/antibody/product/CD32b-Antibody-clone-AT130-2-Monoclonal/12-0321-82>

PE-conjugated Armenian hamster anti-CD16.2 Biologend Cat# 149503
<https://www.biologend.com/en-gb/products/pe-anti-mouse-cd16-2-fcgammariv-antibody-11913?GroupID=BLG13687>

PE-conjugated rat anti-Lyve1 R&D systems Cat# FAB2125P
https://www.rndsystems.com/products/mouse-lyve-1-pe-conjugated-antibody-223322_fab2125p

PE-Cyanine7-conjugated rat anti-Lyve1 Invitrogen Cat# 25-0443-80
<https://www.thermofisher.com/antibody/product/LYVE1-Antibody-clone-ALY7-Monoclonal/25-0443-82>

PE-Cyanine7-conjugated rat anti-F4/80 Invitrogen Cat# 25-4801-82
<https://www.thermofisher.com/antibody/product/F4-80-Antibody-clone-BM8-Monoclonal/25-4801-82>

PE-Cyanine7-conjugated rat anti-CD206 (MMR) Invitrogen Cat# 25-2061-82
<https://www.thermofisher.com/antibody/product/CD206-MMR-Antibody-clone-MR6F3-Monoclonal/25-2061-82>

eFluor660-conjugated rat anti-Lyve1 Invitrogen Cat# 50-0443-82
<https://www.thermofisher.com/antibody/product/LYVE1-Antibody-clone-ALY7-Monoclonal/50-0443-82>

APC-conjugated rat anti-Ly6C Invitrogen Cat# 17-5932-82
<https://www.thermofisher.com/antibody/product/Ly-6C-Antibody-clone-HK1-4-Monoclonal/17-5932-82>

APC-conjugated rat anti-CD16 Biologend Cat# 158005
<https://www.biologend.com/en-gb/products/apc-anti-mouse-cd16-antibody-19298>

APC-conjugated mouse anti-CD64 Biologend Cat# 139306

<https://www.biolegend.com/en-gb/products/apc-anti-mouse-cd64-fcgmamari-antibody-7874?GroupID=BLG8810>

APC-conjugated mouse anti-CD32b Invitrogen Cat# 17-0321-80

<https://www.thermofisher.com/antibody/product/CD32b-Antibody-clone-AT130-2-Monoclonal/17-0321-82>

APC-eFluor780-conjugated rat anti-Gr-1 Invitrogen Cat# 47-5931-82

<https://www.thermofisher.com/antibody/product/Ly-6G-Ly-6C-Antibody-clone-RB6-8C5-Monoclonal/47-5931-82>

AF594-conjugated rat anti-CD31 Biolegend Cat# 102520

<https://www.biolegend.com/en-gb/products/alexa-fluor-594-anti-mouse-cd31-antibody-9633?GroupID=BLG10559>

AF647-conjugated rat anti-CD31 Biolegend Cat# 102516

<https://www.biolegend.com/en-gb/products/alexa-fluor-647-anti-mouse-cd31-antibody-3094>

AF647-conjugated Armenian hamster anti-CD11c Biolegend Cat# 117312

<https://www.biolegend.com/en-gb/products/alexa-fluor-647-anti-mouse-cd11c-antibody-2703>

AF647-conjugated rat anti-B220 BD Pharmingen Cat# 557683

<https://wwwbdbiosciences.com/en-us/products/reagents/flow-cytometry-reagents/research-reagents/single-color-antibodies-ruo/alexa-fluor-647-rat-anti-mouse-cd45r.557683>

AF647-conjugated rat anti-ER-TR7 Novus Biologicals Cat# NB100-64932AF647

https://www.novusbio.com/products/fibroblast-antibody-er-tr7_nb100-64932af647

APC-Cy7-conjugated rat anti-Ly6G BD Pharmingen Cat# 560600

<https://wwwbdbiosciences.com/en-us/products/reagents/flow-cytometry-reagents/research-reagents/single-color-antibodies-ruo/apc-cy-7-rat-anti-mouse-ly-6g.560600>

Brilliant Violet421-conjugated rat anti-F4/80 Biolegend Cat# 123131

<https://www.biolegend.com/fr-ch/products/brilliant-violet-421-anti-mouse-f4-80-antibody-7199?GroupID=BLG5319>

Brilliant Violet605-conjugated rat anti-I-A/I-E Biolegend Cat# 107639

<https://www.biolegend.com/fr-ch/products/brilliant-violet-605-anti-mouse-i-a-i-e-antibody-11988>

Brilliant Violet650-conjugated mouse anti-CX3CR1 Biolegend Cat# 149033

<https://www.biolegend.com/fr-ch/products/brilliant-violet-650-anti-mouse-cx3cr1-antibody-12121>

Goat anti-CGRP Abcam Cat# ab36001

<https://www.abcam.com/en-gb/products/primary-antibodies/cgrp-antibody-ab36001>

Rabbit anti-tyrosine hydroxylase Abcam Cat# ab112

<https://www.abcam.com/en-gb/products/primary-antibodies/tyrosine-hydroxylase-antibody-neuronal-marker-ab112>

Rabbit anti-tub β 3 Abcam Cat# ab18207,

<https://www.abcam.com/en-gb/products/primary-antibodies/beta-iii-tubulin-antibody-neuronal-marker-ab18207>

Biotin-conjugated mouse anti- Ea52-68 peptide bound to I-Ab Invitrogen Cat# 13-5741-82

<https://www.thermofisher.com/antibody/product/Ea52-68-peptide-bound-to-I-Ab-Antibody-clone-eBioY-Ae-YAe-Y-Ae-Monoclonal/13-5741-82>

AF488-conjugated mouse anti-alpha smooth muscle actin Abcam Cat# AB184675

<https://www.abcam.com/en-gb/products/primary-antibodies/alexa-fluor-488-alpha-smooth-muscle-actin-antibody-1a4-ab184675>

AF594-conjugated donkey anti-guinea Pig Jackson ImmunoResearch Cat# 706-585-148

<https://www.jacksonimmuno.com/catalog/products/706-585-148>

AF594-conjugated mouse anti-CD31 Biolegend Cat# 303126

<https://www.biolegend.com/en-gb/products/alexa-fluor-594-anti-human-cd31-antibody-10182?GroupID=BLG10311>

AF647-conjugated mouse anti-CD55 Novus Biologicals Cat# NBP2-47964AF647

https://www.novusbio.com/products/cd55-daf-antibody-143-30_nbp2-47964af647

AF647-conjugated mouse anti-HLA-DR Abcam Cat# ab223907

<https://www.abcam.com/en-gb/products/primary-antibodies/alexa-fluor-647-hla-dr-antibody-tal-1b5-ab223907>

Goat anti-CD32B Abcam Cat# AB77093

<https://www.abcam.com/en-gb/products/primary-antibodies/cd32b-antibody-ab77093>

Goat anti-LYVE1 R&D systems Cat# AF2089

https://www.rndsystems.com/products/human-lyve-1-antibody_af2089

Rabbit anti-PLVAP Novus Biologicals Cat# NBP1-83911

https://www.novusbio.com/products/plvap-antibody_nbp1-83911

Rabbit anti-LYVE1 Abcam Cat# ab33682

<https://www.abcam.com/en-gb/products/primary-antibodies/lyve1-antibody-ab33682>

PE/Dazzle594-conjugated mouse anti-CD206 Biologend Cat# 321130
<https://www.biologend.com/en-gb/products/pe-dazzle-594-anti-human-cd206-mmr-antibody-13265?GroupID=BLG4585>

Anti-mouse CSF1R (CD115) Biocell Cat# BE0213
<https://biocell.com/invivomab-anti-mouse-csf1r-cd115-be0213>

Anti-mouse TNF α Biocell Cat# BE0058
<https://biocell.com/invivomab-anti-mouse-tnf-alpha-be0058>

Anti-mouse CXCL1 R&D systems Cat# MAB453
https://www.rndsystems.com/products/mouse-cxcl1-groalpha-kc-cinc-1-antibody-48415_mab453

Anti-mouse IL-1 β Invivogen Cat# mil1b-mab9-02
<https://www.invivogen.com/recombinant-anti-mouse-il1beta-antibody>

Validation data of Guinea pig anti-NP2 is provided in Supplementary fig. 9.

Eukaryotic cell lines

Policy information about [cell lines and Sex and Gender in Research](#)

Cell line source(s)	HEK293 tsA201 cells were kindly gifted from R. Horn, Thomas Jefferson University, Philadelphia, USA.
Authentication	Authentication has originally been performed by the provider.
Mycoplasma contamination	Cell lines were regularly tested for mycoplasma contamination.
Commonly misidentified lines (See ICLAC register)	<i>Name any commonly misidentified cell lines used in the study and provide a rationale for their use.</i>

Animals and other research organisms

Policy information about [studies involving animals; ARRIVE guidelines](#) recommended for reporting animal research, and [Sex and Gender in Research](#)

Laboratory animals	Wild-type mice (C57BL/6J background) were bred in-house or purchased from Jackson Laboratories (Margate, UK). Transgenic mice expressing Venus EYFP under the control of the CD11c promoter were a gift from M Nussenzweig (Rockefeller University, New York, New York, USA). Fcgr2b $^{-/-}$ mice were kindly provided by J. Ravetch (Rockefeller University) and S. Bolland (US National Institutes of Health, US National Institute of Allergy and Infectious Diseases (NIAID)). CX3CR1-cre/ERT2: IL-1 β flox mice were provided by Dr. Denes. Both male and female mice were used. For in vivo experiments, 8- to 20-week-old mice were used unless mentioned. Mice were maintained in specific pathogen-free conditions at a Home Office-approved facility with controlled humidity and temperature with a light/dark cycle of 12h each in the UK.
Wild animals	No wild animals were involved.
Reporting on sex	Both female and male mice were used in the study and no sex difference was confirmed.
Field-collected samples	No samples were collected from the field.
Ethics oversight	All procedures were ethically approved by the University of Cambridge Animal Welfare and Ethical Review Body and carried out in accordance with the United Kingdom Animals (Scientific Procedures) Act of 1986 under the authority of a UK Home Office Licence.

Note that full information on the approval of the study protocol must also be provided in the manuscript.

Plants

Seed stocks	<i>Report on the source of all seed stocks or other plant material used. If applicable, state the seed stock centre and catalogue number. If plant specimens were collected from the field, describe the collection location, date and sampling procedures.</i>
Novel plant genotypes	<i>Describe the methods by which all novel plant genotypes were produced. This includes those generated by transgenic approaches, gene editing, chemical/radiation-based mutagenesis and hybridization. For transgenic lines, describe the transformation method, the number of independent lines analyzed and the generation upon which experiments were performed. For gene-edited lines, describe the editor used, the endogenous sequence targeted for editing, the targeting guide RNA sequence (if applicable) and how the editor was applied.</i>
Authentication	<i>Describe any authentication procedures for each seed stock used or novel genotype generated. Describe any experiments used to assess the effect of a mutation and, where applicable, how potential secondary effects (e.g. second site T-DNA insertions, mosaicism, off-target gene editing) were examined.</i>

Plots

Confirm that:

- The axis labels state the marker and fluorochrome used (e.g. CD4-FITC).
- The axis scales are clearly visible. Include numbers along axes only for bottom left plot of group (a 'group' is an analysis of identical markers).
- All plots are contour plots with outliers or pseudocolor plots.
- A numerical value for number of cells or percentage (with statistics) is provided.

Methodology

Sample preparation

After sacrifice under anaesthesia, the right auricles of the mice were cut and 10 ml of pre-warmed 1x PBS was injected into the left ventricle for perfusion. Perfusion was omitted in experiments designed to assess blood samples. After removal of the skin, the quadriceps femoris muscles were carefully removed. The attachment of synovium to the bare area of femur was observed by pinching and lifting up the patella with tweezers under a stereoscopic microscope (Stemi 2000-CS, Zeiss). The bone-synovium and the meniscus-synovium interface is carefully dissected throughout knee joint without damaging the bone, and patella is removed at the end. For flow cytometry analysis, whole mount synovial tissues were digested with 2 mg/ml type I collagenase in RPMI and incubated at 37°C for 45 min. Disaggregated tissue elements were passed through a 70 µm cell strainer. Measurements were performed on an CytoFLEX LX (Beckman Coulter) and analyzed with FlowJo software (Tree Star). Sorting was performed on an FACSARIA Fusion (Becton Dickinson). Single cell suspensions were incubated with Zombie Aqua (Biolegend) or Viakrome 808 fixable viability dye (Beckman Coulter) diluted 1:250 in PBS for 15 minutes at 4°C. Samples were centrifuges, resuspended in FACS buffer with anti-CD16/32 antibody (Biolegend) diluted 1:50 in FACS buffer, followed by staining with the antibodies for 15 minutes at 4°C.

Instrument

CytoFLEX LX (Beckman Coulter) for FACS, FACSARIA Fusion (Becton Dickinson) for cell sorting.

Software

FlowJo version 10.6.2 was used for data analysis.

Cell population abundance

Cell populations were abundant enough for any of the analysis. Approximately over 200 cells of each target cell population were detected from the synovium per mouse and we compiled multiple mice when needed.

Gating strategy

The initial gate on FSC/SSC plots was set to remove cell debris and single cells were gated according to FSC-W and FSC-H. After gating on live cells using ViaKrome 808, target cell populations were gated as depicted in Supplementary Fig. 3c.

- Tick this box to confirm that a figure exemplifying the gating strategy is provided in the Supplementary Information.